

## Cell size and nuclear scaling relationships in multinucleated muscle fibers

Stefanie E. Windner<sup>1</sup>, Angelika Manhart<sup>2</sup>, Amelia Brown<sup>1</sup>, Alex Mogilner<sup>2</sup>, Mary K. Baylies<sup>1\*</sup>

<sup>1</sup>Developmental Biology Program, Sloan Kettering Institute, Memorial Sloan Kettering Cancer Center, New York, NY 10065

<sup>2</sup>Courant Institute, New York University, New York, NY 10012

\*Corresponding author (m-baylies@ski.mskcc.org)

### Key words

Nuclear Scaling, Cell Size, Skeletal Muscle, Nuclear Coordination, Nuclear Compensation, Nuclear synthetic activity, Nuclear positioning, Syncytial organization, Polyploidy, Drosophila

### Highlights

- Muscle nuclei coordinately establish linear scaling relationships with cell size
- Nuclear positioning regulates individual nuclear sizes
- Nuclear synthetic activity is inversely correlated with nuclear size scaling
- Precise nuclear scaling is required for muscle function

## SUMMARY

Optimal cell performance depends on cell size and the appropriate relative size, i.e. scaling, of the nucleus. How nuclear scaling is regulated and contributes to cell function is poorly understood, especially in skeletal muscle fibers, which are among the largest cells, containing hundreds of nuclei. Here we present a *Drosophila* *in vivo* system to analyze nuclear scaling in whole multinucleated muscle fibers, genetically manipulate individual components, and assess muscle function. Despite precise global coordination, we find that individual nuclei within a myofiber establish different local scaling relationships by adjusting their size and synthetic activity in correlation with positional/spatial cues. While myonuclei exhibit compensatory potential, even minor changes in global nuclear size scaling correlate with reduced muscle function. Our study provides the first comprehensive approach to unraveling the intrinsic regulation of size in multinucleated muscle fibers. New insights to muscle cell biology will accelerate the development of interventions for muscle diseases.

## INTRODUCTION

The physical dimensions of a cell and the appropriate relative size of its organelles are essential for cell structure and function. In particular, the size of the nucleus is adjusted proportionally to cell size to accommodate specialized cell functions and metabolic demands. Nuclear size is determined by several factors, including DNA content, chromatin compaction, and nuclear transport, which in turn affect gene expression and nuclear mechanics (Levy and Heald, 2012). Ultimately, each cell type can be characterized by a specific ratio of nuclear to cytoplasmic volume (nuclear size scaling) (Conklin, 1912). Changes in nuclear size scaling are routinely used as diagnostic indicator for a variety of disease states (Jevtić and Levy, 2014); however, the intracellular mechanisms that coordinate different nuclear components and activities to establish and maintain specific cell sizes remain largely elusive.

Skeletal muscle fibers are one of the largest cell types and possess remarkable cell size plasticity. Individual cells develop and grow by fusion of myoblasts and can contain hundreds of nuclei distributed across the cell surface (Deng et al., 2017). Based on the limited synthetic capacity of a single nucleus and the physical limitations to cellular transport and diffusion, a longstanding hypothesis (known as myonuclear domain hypothesis) postulates that, each nucleus in a muscle syncytium only supplies its immediately surrounding cytoplasm with gene products (Hall and Ralston, 1989; Pavlath et al., 1989). Accordingly, studies using different muscle systems have suggested that muscle nuclei are positioned to minimize transport distances throughout the cytoplasm (Bruusgaard et al., 2003; Manhart et al., 2018). As a result, the number of myonuclei is considered the main determinant of overall muscle cell size. However, nuclear numbers vary depending on factors like muscle fiber type, activity, or age, indicating that the average size of the cytoplasmic domain associated with each nucleus is highly variable (Van der Meer et al., 2011). Further, differences exist within a muscle fiber in nuclear density and/or gene expression, particularly in nuclei adjacent to specialized sub-cellular structures like muscle attachment sites (myotendinous junctions, MTJs) and the motoneuron synapse (neuromuscular junction, NMJ) (Bruusgaard et al., 2003; Rosser and Bandman, 2003). While this suggests that muscle nuclei can adjust their synthetic activity dependent on cell size and functional demands (K. Gundersen, 2016), it is still not clear how the contribution of individual nuclei to cell size is coordinated in a shared cytoplasmic space and whether nuclear size scaling plays a role in regulating muscle fiber size.

Diseases of the skeletal musculature are commonly associated with changes in nuclear positioning, nuclear sizes, and nuclear activities, but how different muscle phenotypes result in reduced muscle function remains poorly understood. The size and the complexity of muscle tissue in vertebrates impose technical challenges that limit most studies on fiber size and intracellular organization to tissue cross-sections or *in vitro* approaches. To provide a more comprehensive understanding of nuclear scaling relationships and the intrinsic regulation of cell size in multinucleated muscle fibers, we have developed a *Drosophila* *in vivo* system to quantify cell and nuclear parameters in fully differentiated muscle cells, genetically manipulate individual cellular components, and evaluate muscle function. This system allowed us to analyze nuclear scaling relationships on a global level (scaling of the cumulative nuclear content with total cell size) and a local level (scaling of individual nuclei with their surrounding cytoplasmic domain), and identify possible mechanisms of nuclear coordination and compensation within individual muscle fibers.

## RESULTS

### Quantification of cell and nuclear sizes

The body wall musculature of the *Drosophila* larva is a well-established system to investigate fundamental aspects of muscle cell biology (Demontis et al., 2013; Deng et al., 2017; H Keshishian et al., 2003; Piccirillo et al., 2014). The musculature is comprised of 30 different muscles, which are arranged in the same stereotyped pattern in every abdominal hemisegment (Schulman et al., 2015). Each of these glycolytic muscles consists of only one multinucleated cell with distinct size, shape, and attachment sites, and is easily accessible in live or dissected preparations (Dobi et al., 2015). Here we focused on two muscles, Ventral Longitudinal muscles VL3 and VL4 (also known as muscles 6 and 7), which are consistently flat rectangular cells with disc-shaped nuclei located on only one cell surface (Figures 1A and 1B). To assess a range of VL muscle sizes, we used larvae from three genetic control backgrounds and quantified VL3 and VL4 muscles in abdominal hemisegments 2-6 within each larva. We compared 2D and 3D quantification of cell and nuclear sizes, and found that this system, due to its morphological simplicity, allowed for quantification of size on projections of confocal z-stacks (Figures 1C and 1D). On average, VL3 muscles are almost twice the size of VL4 muscles, with comparable sizes across individual larvae and genotypes (VL3:  $39658 \pm 7622 \mu\text{m}^2$ , VL4:  $25581 \pm 3643 \mu\text{m}^2$ ; Figures 1E). Within each larva,

VL3 muscles are significantly bigger in the anterior hemisegments 2-4 and approximated the size of VL4 muscles in more posterior hemisegments (Figure 1F). In contrast, VL4 muscle size is consistent along the anterior-posterior axis of the larvae. Together, VL3 and VL4 muscles provide a significantly different, but overlapping, range of cell sizes. To further validate our dataset, we performed unsupervised cluster analysis using the following parameters: cell area, cell shape (aspect ratio: length/width), cell position (abdominal hemisegment number), number of nuclei, and cumulative nuclear area. Clustering divides the data into two groups that do not show any bias for individual larvae, genotypes or experimental replicates (Figure S1A), but clearly correspond to VL3 and VL4 muscles (Figure 1G). Thus, VL3 and VL4 muscles are comparable across larvae and different genotypes, but inherently different when compared to each other.

### **Muscle nuclei establish precise global scaling relationships with cell size**

To achieve a comprehensive characterization of “nuclear scaling” with regard to the cell size of multinucleated VL muscle fibers, we quantified 4 global nuclear parameters: number of nuclei, cumulative DNA content (nuclear ploidy), cumulative area of all nuclei, and cumulative area of all nucleoli (Figures 2A-2C). All parameters showed linear scaling with cell size across VL muscle types, however, with different linear fits (Figures 2D-2G). Nuclear numbers ranged from 9-21 in VL3 and from 6-13 in VL4, with a considerable range of cell sizes for every given number of nuclei (Figure 2D, correlation coefficient  $R=0.74$ ). During *Drosophila* development, fusion of embryonic myoblasts initially sets the number of nuclei per muscle fiber. Subsequently endoreplication increases the DNA content within each nucleus to promote muscle growth in the larva (Demontis and Perrimon, 2009). To independently assess the DNA content in VL muscles, we calculated nuclear ploidy numbers based on Hoechst fluorescence intensities in diploid muscle progenitor cells (AMPs, Figures 2C and S1B-S1D): VL3 muscles contain a total of  $614+/-153$  copies, VL4 muscles a total of  $386+/-96$  copies of DNA. Notably, cells with the same number of nuclei contain different amounts of cumulative DNA content, resulting in improved linear scaling with cell area compared to nuclear number (Figure 2E,  $R=0.86$ ). The cumulative area of all nucleoli showed linear scaling with VL cell size similar to DNA content (Figure 2G,  $R=0.88$ ), while the cumulative area of all nuclei showed the best linear correlation with cell area across both VL muscle types (Figure 2F,  $R=0.90$ ). These data indicated that multinucleated muscle fibers establish precise global nuclear scaling relationships, which suggested a high level of coordination

among the nuclei contained within a cell.

To directly compare muscle fibers with varying nuclear numbers, we normalized all global parameters by the number of nuclei per cell, thereby calculating the average size of the cytoplasmic domain per nucleus (cell area/nuclear number), the average DNA content per nucleus (cumulative DNA content/nuclear number), and the average size of nuclei and nucleoli (cumulative area/nuclear number). Average cytoplasmic domain sizes showed a similar distributions and range in VL3 and VL4 muscles (Figure 2H), suggesting a similar “optimal” cytoplasmic domain size per nucleus in both VL muscles. The average DNA content per nucleus increased linearly with average cytoplasmic domain size (Figure 2I), indicating that endoreplication amplifies nuclear ploidies in correlation with the number of nuclei available for a certain cell size. Similarly, average nuclear and nucleolar areas showed a linear increase with average cytoplasmic domain size (Figures S1E and S1F). To further investigate global size scaling of nuclei and nucleoli, we calculated the percentage of cumulative nuclear and nucleolar area per cell area. Strikingly, VL3 and VL4 muscles with a similar average DNA content established significantly different nuclear and nucleolar size scaling relationships (Figures 2J, 2K, S1G, S1H). Given the function of the nucleolus in ribosome biogenesis, and consequently cell growth and size control (Conklin, 1912), proportionally larger nuclei and nucleoli in VL3 muscles indicated overall higher metabolic demands per nucleus.

Together these data demonstrated that a variety of global nuclear parameters scale with the size of multinucleated muscle fibers; however, the cumulative size of all nuclei gives the best prediction of muscle cell size. We propose that global nuclear scaling with VL muscle size is achieved in three steps: firstly, the number of nuclei sets a range of possible cell sizes; secondly, each cell during growth individually increases nuclear ploidies to maintain a stable scaling of cumulative of DNA content with cell size. Thirdly, the size of nuclei and nucleoli is continuously adjusted, similar to mononucleated/diploid cells, to establish precise, cell type specific scaling with cell size and allow for optimal cell function.

### **Nuclear positioning regulates individual nuclear sizes**

The accuracy of global nuclear scaling in multinucleated VL muscles suggested that the nuclei contained within a cell are highly coordinated. We hypothesized that stable global scaling relationships are established via local scaling of individual nuclei with their surrounding

cytoplasmic domain. To test this, we determined nuclear positions within each cell based on their centroids, and thus independent of their size (Figure 3A). In both VL muscles, the distances between nuclei (Nearest Neighbor Distances) were larger than expected for random distribution, confirming that nuclei are deliberately positioned (Figure S2A). Along the length of each fiber, nuclei were organized in rows, typically two rows in VL3 and one row in VL4 muscles (Figure 3B). However, in VL3 and VL4 muscles with the same geometric properties (cell dimensions, number of nuclei) the number and the position of rows were similar (Figure 3C and S2B), indicating that geometrical factors, rather than VL muscle type, dictate the nuclear patterns.

In *Drosophila* and mammalian muscle fibers, nuclear positioning involves microtubules and motor proteins to generate mechanical forces (Folker and Baylies, 2013; G. G. Gundersen and Worman, 2013; Roman and Gomes, 2017). In larval VL3 and VL4 muscles, microtubules emanate from the nuclear envelopes and form an array surrounding each nucleus (Figure S2C). We performed mathematical simulations to test whether mechanical forces associated with each nucleus were sufficient to explain nuclear positioning in VL3 and VL4 muscles independent of nuclear sizes (see methods). In brief, we used experimental data (cell dimension, nuclear number, positions) as the initial condition and assumed that nuclei interact with each other and with the cell edges via repulsive forces (Figure 3D). The simulated data shown in Figures 3B, 3C, and S2 (force  $\sim 1/\text{distance}^2$ , force ratio between inter-nuclear and nuclear-cell edge interactions  $q=0.7$ ) clearly recapitulated nuclear positioning in both VL3 and VL4 muscles. The close approximation of simulated positions with real data suggested that similar mechanisms, based on cell geometry and mechanical forces, establish a force balance to position nuclei in VL3 and VL4 muscles, independent of absolute cell and nuclear sizes.

If nuclei are positioned via mechanical interactions yet independent of their size, we hypothesized that these nuclei assess the size of their surrounding cytoplasmic domain and adjust their own size, to establish local size scaling relationships. To further investigate this possibility, we simulated a space-sensing mechanism, which predicts the size of each nucleus based on the detected amount of a hypothetical diffusible cytoplasmic molecule at a given position within the cell (see methods). Using real cell shapes and nuclear positions, our simulations predicted nuclear areas that correlated linearly with the biological data (Figure 2E). These data indicate that local space sensing could be involved in regulating nuclear sizes within each cell.

Our space-sensing model predicts correlations between the size of individual nuclei and

the size of their surrounding cytoplasmic domain. To test this *in vivo*, we used an unbiased approach to geometrically partition each cell into cytoplasmic domains based on nuclear positions (Voronoi tessellation (Du et al., 2010), Figure 3A). In accordance with our simulations, we found a linear correlation between nuclear and Voronoi areas in both VL muscle types. However, in contrast to the precise global nuclear size scaling relationships (Figure 2G, R=0.90), the local correlation of nuclear size and cytoplasmic domain size was much weaker (Figure 3F, R=0.55). Closer analysis of nuclear sizes revealed that within both VL muscle types, nuclei located at the cell ends are considerably smaller than nuclei in the cell middle, while Voronoi domain sizes are more consistent along the length of the muscle fibers (Figures 3G and 3H). Multiple linear regression analyses using various cell parameters confirmed that the best prediction of nuclear size was achieved by a combination of local cytoplasmic domain area and nuclear position along the length of the muscle fiber (Figure 3I, R=0.66, p<0.0001). This demonstrated that individual VL muscle nuclei established local size scaling relationships; however, each cell contained a heterogeneous population of nuclei with different sizes. In addition to the size of the cytoplasmic domain, similar regionally restricted signals regulate nuclear sizes within each VL muscle.

Together these data suggested that VL nuclei are coordinated, via a force balance, to evenly distribute throughout the cells and establish stable global scaling relationships by adjusting their size based on local spatial parameters, which consistently vary along the length of each muscle fiber.

#### **Local nuclear size scaling and synthetic activity are inversely correlated**

The specific pattern of nuclear sizes along each cell resulted in similar local nuclear size scaling differences (% nuclear area per Voronoi area) along VL3 and VL4 muscles. Strikingly, the position of the neuromuscular junction (NMJ) correlated with the highest nuclear size scaling values in both VL muscles, while nuclei adjacent to the anterior and posterior myotendinous junctions (MTJs) showed significantly lower values (Figures 4A, 4B, S3A). Thus, within each muscle fiber, nuclear size scaling differences correlated with regions associated with specific cell functions during muscle contraction.

To determine whether nuclear ploidy affects local scaling of nuclear size with Voronoi domain size, we calculated DNA copy numbers for each nucleus (Figures 3C and S1). We identified nuclei with 16, 32, or 64 copies of DNA, which on average, occurred at a similar

frequency in VL3 and VL4 muscles. However, each cell established a distinct ratio of nuclear ploidy numbers in correlation with the number of nuclei and cell size, so that cells with larger average cytoplasmic domain sizes contained a higher percentage of 64c nuclei (Figure 4D). Along each VL fiber, 16c nuclei were located adjacent to the MTJs, 32c were positioned throughout the cell, and 64c were located mainly in the cell center (Figure 4E). We compared size parameters associated with 32c and 64c nuclei: a doubling in DNA content correlated with significant increases in mean nuclear area (35%) and cytoplasmic domain area (21%). Thus, on average, local nuclear size scaling was increased for 64c nuclei (Figure 4F). These data suggested that systemic growth signals are differentially interpreted by individual nuclei dependent on their position within the cell, and that DNA content affects absolute nuclear sizes, as well as local nuclear size scaling. However, both 32c and 64c nuclei established a similar size scaling pattern along the muscle fibers (Figure S3B and S3C), indicating that regional scaling differences are established independent of absolute nuclear DNA content.

Regional differences in nuclear sizes and DNA content suggested significant local differences in nuclear synthetic activity within each muscle fiber. We quantified nucleolar sizes and determined local nucleolar scaling (% nucleolar area per nucleus) as readout for the relative synthetic activity of individual nuclei (Figure 2C). Locally, nucleolar areas showed a better linear correlation with nuclear areas than with Voronoi domain sizes and were significantly larger (24%) in 64c nuclei (Figures 4F, S3D, S3E). However, local nucleolar scaling was increased in 32c nuclei, indicating proportionally higher nuclear synthetic activity in nuclei containing less DNA. Along the muscle cells, nucleolar scaling showed significant regional differences independent of absolute DNA content and VL muscle type (Figures 4G, S3F, S3G). Intriguingly, the pattern of local nucleolar scaling was inverted compared to local nuclear size scaling along the muscle fibers (Figure 3H), so that the smallest nuclei at the anterior MTJ contained proportionally large nucleoli. Together these data indicated that nuclear synthetic activity compensates for differences in nuclear DNA content, as well as for differences in local nuclear size scaling.

To independently assess nuclear synthetic activity, we analyzed labeling of H3K9ac, a conserved marker of gene activation (Boros, 2012). H3K9ac fluorescence intensities indicated that the number of active transcriptional start sites increased proportional with nuclear ploidy; normalizing by DNA content, however, resulted in similar relative H3K9ac levels in 16c, 32c and 64c nuclei (Figures 4I and 4J). Within each muscle fiber, H3K9ac showed clear regional

differences, similar to nucleolar size scaling (Figure 4K). Thus, individual nuclei establish specific/distinct combinations of nuclear size and synthetic activity along the length of each muscle fiber, independent of absolute local DNA content.

Together these data showed that within each muscle fiber, regions associated with different cell functions are characterized by differences in DNA content, nuclear size scaling, and nuclear synthetic activity. In mononucleated cells, DNA content limits the number of nucleolar components like Fibrillarin, and nucleolar size establishes in a concentration-dependent manner within the nucleus (Brangwynne, 2013; Ma et al., 2016; Uppaluri et al., 2016; Weber and Brangwynne, 2015). If muscle nuclei contribute to a shared pool of nucleolar components with even distribution throughout the cytoplasm, smaller nuclei containing less DNA would import a proportionally increased number nucleolar components and form proportionally larger nucleoli. We propose that in VL muscles fibers, nuclear size scaling and synthetic activity are a directly linked via inverse scaling of the nucleolus. This mechanism would allow local differences in nuclear sizes and DNA content, while maintaining similar cytoplasmic domain sizes along each muscle fiber and stable global cell size regulation.

### **Nuclear compensation and functional consequences**

Our analyses suggested that DNA content affects the absolute size of cells, nuclei, and nucleoli, while nuclear positioning and local size scaling are regulated independent of nuclear ploidy. To test our assumptions and investigate the robustness of nuclear scaling and cell function, we genetically manipulated the DNA content in the larval musculature. We knocked down a component of the DNA replication machinery (*Dmef2 > ctd1(dup)RNAi*) to reduce the amount of endoreplication (Whittaker et al., 2000), and overexpressed a regulator of cell cycle progression (*Dmef2 > dMyc*) to promote endoreplication specifically in muscle during larval growth (Pierce et al., 2004). These manipulations resulted in significant differences in nuclear DNA content: *Cdt(Dup)* knockdown (KD) reduced nuclear ploidy numbers by one round of endoreplication (8c, 3%; 16c, 83%; 32c, 14%), whereas *Myc* overexpression (OE) increased nuclear ploidies by approximately one round of endoreplication (32c, 6%; 64c, 38%; 128c, 55%; 256c, 1%) (Figures 5A and S4A). *Cdt1(Dup)KD* muscles were only ~10% smaller, and *MycOE* muscles had similar cell sizes compared to controls (Figures 5B and S4B), indicating that the changes in cumulative DNA content did not override the systemic demands for a specific muscle size. However, larval

locomotion was significantly reduced in both genotypes (Figure 5B), suggesting that changes in nuclear scaling negatively affect muscle function.

We analyzed global nuclear scaling relationships and found that Cdt1(Dup)KD and MycOE did not affect the number of VL nuclei, thus scaling of nuclear number with cell size was similar to control muscles (Figures 5C and S4C). Further, global linear scaling of DNA content, nuclear and nucleolar areas with cell size across VL3 and VL4 muscles types was maintained in Cdt1(Dup)KD and MycOE backgrounds, despite changes in absolute parameters (Figures 5D-5F). On average, Cdt1(Dup)KD resulted in a 62% reduction in total DNA content, and 60% reduction in cumulative nucleolar areas, while the cumulative area of all nuclei was only 25% smaller than in control cells (Figures S4D-F). Thus, Cdt1(Dup)KD nuclei compensated by increasing their size relative to DNA content, but small nucleolar sizes indicated that synthetic activity was not upregulated (no compensation). In fact, cumulative nucleolar sizes were highly correlated with total DNA content (Figure 5G), indicating that the amount of nuclear DNA could limit absolute nucleolar sizes within each cell. In contrast to Cdt1(Dup)KD, MycOE resulted in a doubling in cumulative DNA content, a four-fold increase in cumulative nucleolar area, and a doubling in cumulative nuclear areas (Figures S4D-F). Despite a dramatic increase in nucleolar areas, MycOE nuclei maintain a linear scaling of nuclear sizes with DNA content similar to control cells (Figure 5H). Together these data suggest that nuclei regulate their size within a range set by DNA content yet differentially respond to increases and decreases in nuclear ploidy. In addition to limitations of the synthetic machinery, it is possible that chromatin compaction and mechanical properties of the nucleus limit the range of nuclear size adjustments in dynamically contracting muscle fibers.

In accordance with our simulations of nuclear positioning in control cells, Cdt1(Dup)KD and MycOE nuclei were properly positioned despite different nuclear sizes (Figures S4G and S4H). Further, in both genotypes DNA ploidy numbers and nuclear sizes were smallest adjacent to the MTJs and increased towards the cell center (Figures S4I and S4J). Strikingly, the relative distribution of nuclear sizes along each cell was similar in MycOE, Cdt1(Dup)KD, and control muscles (Figure 5I), suggesting that regional patterning mechanisms were intact and regulate nuclear size differences rather than absolute nuclear sizes within each cell. In MycOE muscles, upregulation of the synthetic machinery resulted in a loss of the coordination between local nuclear scaling and synthetic activity within the cells (Figure 5J). In Cdt1(Dup)KD muscles, the inverse relationship between local nuclear and nucleolar size scaling was maintained along the cells,

despite overall smaller nuclei and nucleoli (Figure 5J). These data confirm that nuclei contained within the same muscle fiber are highly coordinated and support the idea that DNA content regulates absolute nuclear sizes and synthetic activity, while nuclear positioning mechanisms and functionally distinct regions within each cell determine the relative contribution of individual nuclei to cell size.

Together, these experiments highlight different levels of muscle size regulation in multinucleate muscle fiber (Figure 6), demonstrate the robustness of intracellular organization, and stress the importance of nuclear scaling for muscle cell function.

## DISCUSSION

Skeletal muscle fibers are large multinucleated cells with remarkable size plasticity. Our study provides the first comprehensive analysis of cell size and nuclear scaling relationships in whole, fully differentiated muscle fibers using a large *in vivo* dataset. We show that nuclear scaling is essential for muscle function and depends on local factors (cytoplasmic domain size), regional factors (proximity to NMJ, MTJs), as well as global factors (muscle type) (Figure 6).

On the global level, a variety of nuclear parameters scale with muscle cell size, including nuclear number, DNA content, nucleolar size, and nuclear size. The correlation of nuclear number and DNA content with muscle cell size has been appreciated in a variety of systems, however nuclear size scaling has not been previously investigated in muscle fibers. The precision of global nuclear and nucleolar size scaling in VL muscles is reminiscent of mononucleated cells, where cell-type specific scaling of the nucleus and nucleolus are associated with optimal cell function (Levy and Heald, 2012). Strikingly, VL3 and VL4 muscles establish distinct global nuclear and nucleolar size scaling, indicating that size scaling relationships are established in a muscle type specific manner. While the consequences of size scaling differences in wild-type *Drosophila* muscles remain to be determined, it is possible that nuclear and nucleolar size scaling are indicative of the differences in functional demands observed in different vertebrate muscle fiber types.

The global nuclear scaling relationships uncovered in our study rest on the coordination of the nuclei within each muscle fiber. Our data indicate that VL muscle nuclei are actively positioned via mechanical forces and based on cell geometries, which results in similar

cytoplasmic domain sizes throughout the cell. Similar findings in mouse muscle fibers suggest that the mechanisms of nuclear positioning are conserved across species (Bruusgaard et al., 2003). While increasing domain sizes during muscle growth (hypertrophy) in mice trigger increase in DNA content via cell fusion (Qaisar and Larsson, 2014), *Drosophila* larval muscle nuclei undergo endoreplication to maintain stable scaling of total DNA content with cell size. Why DNA content and nuclear scaling show regional differences along the muscle fibers remains to be determined; however, it is likely that, as in mammals, NMJs and MTJs impose distinct functional requirements on adjacent nuclei. Experiments aimed at identifying the molecular mechanisms regulating these intracellular patterning and scaling relationships are underway and will provide valuable insights to the biology and physiology of muscle cells, as well as other multinucleated cell types such as trophoblasts and osteoclasts.

Cell size regulation is highly coordinated among all nuclei contained within a muscle fiber, yet individual nuclei distinctly contribute to size. While the existence of distinct myonuclear domains has been previously suggested (Hall and Ralston, 1989; Pavlath et al., 1989; Van der Meer et al., 2011), the extent of nuclear diversity and the precision of nuclear patterning within individual fibers and on population level have not been documented. We propose that muscle fibers are composed of a mosaic of cytoplasmic domains, whereby each nucleus integrates a variety of spatial/location signals and locally coordinates its DNA content, nuclear size scaling, and synthetic activity. Studies in mononucleated cells have shown that DNA content limits the number of nucleolar components, like Fibrillarin, and that nucleolar sizes establish in a concentration-dependent manner within the nucleus (Brangwynne, 2013; Ma et al., 2016; Uppaluri et al., 2016; Weber and Brangwynne, 2015). We find that the total DNA content regulates the cumulative size of nucleoli within VL muscle fibers. If each muscle nucleus contributes to a shared pool of nucleolar components with even distribution throughout the cytoplasm, smaller nuclei would import an increased number nucleolar components and form proportionally larger nucleoli. This inverse coupling of nuclear size and synthetic activity via the relative size of the nucleolus represents a possible mechanism that compensates for different local requirements in nuclear synthetic activity, while maintaining stable global cell size regulation in a syncytial cell.

While the molecular mechanisms of nuclear size regulation await further investigation, our study represents an important step toward optimizing the quantification of muscle cell size and understanding the complex mechanisms of intracellular size regulation in multinucleated cells. In

this regard, our data should affect our thinking on the quantification of muscle cell size, as well as on therapies aimed at regulating muscle growth, homeostasis, and regeneration. Ultimately, identifying the regulatory network that coordinates intracellular size regulation in multinucleated muscle fibers will reveal how disruption of sub-cellular organization results in muscle disease and reduced muscle function.

## Acknowledgements

We would like to thank Terry Orr-Weaver, Norbert Perrimon, and the Bloomington Stock Center for flies. We acknowledge Raya Khanin in the MSKCC Bioinformatics core for the PCA analysis. We would also like to thank members of the Baylies Lab for helpful discussion, and particularly Mafalda Azevedo for critical reading of the manuscript. This work was supported by the NIH [GM121971, AR068128] to MKB and National Cancer Institute [P30 CA 008748] core grant to MSKCC. The funders had no role in the study design, data collection and analysis, decision to publish, or preparation of the manuscript.

## Author contributions

S.W., M.B., A.M., and A.M. conceived the experiments; S.W. and A.M. carried them out; S.W. and A.M., with input from A.M. and M.B., designed and carried out the data analysis; A.B. and S.W. automated the larval data analysis; A.B. performed area/volume analysis. S.W., A.M., A.M., and M.B. prepared the manuscript.

## Competing interests

We have no competing interests to declare.

## References

- Boros, I.M., 2012. Histone modification in drosophila. *Briefings in Functional Genomics* 11, 319–331. doi:10.1093/bfgp/els029
- Brangwynne, C.P., 2013. Phase transitions and size scaling of membrane-less organelles. *The Journal of cell biology* 203, 875–881. doi:10.1083/jcb.201308087
- Bruusgaard, J.C., Liestøl, K., Ekmark, M., Kollstad, K., Gundersen, K., 2003. Number and spatial distribution of nuclei in the muscle fibres of normal mice studied in vivo. *The Journal of Physiology* 551, 467–478. doi:10.1113/jphysiol.2003.045328
- Conklin, E.G., 1912. Cell size and nuclear size. *Journal of Experimental Zoology* 12, 1–98. doi:10.1002/jez.1400120102
- Demontis, F., Perrimon, N., 2009. Integration of Insulin receptor/Foxo signaling and dMyc activity during muscle growth regulates body size in Drosophila. *Development (Cambridge, England)* 136, 983–993. doi:10.1242/dev.027466
- Demontis, F., Piccirillo, R., Goldberg, A.L., Perrimon, N., 2013. Mechanisms of skeletal muscle aging: insights from Drosophila and mammalian models. *Dis Model Mech* 6, 1339–1352. doi:10.1242/dmm.012559
- Deng, S., Azevedo, M., Baylies, M., 2017. Acting on identity: Myoblast fusion and the formation of the syncytial muscle fiber. *Seminars in Cell & Developmental Biology* 72, 45–55. doi:10.1016/j.semcd.2017.10.033
- Dobi, K.C., Schulman, V.K., Baylies, M.K., 2015. Specification of the somatic musculature in Drosophila. *Wiley interdisciplinary reviews. Developmental biology* 4, 357–375. doi:10.1002/wdev.182
- Du, Q., Gunzburger, M., Ju, L., 2010. Advances in studies and applications of Centroidal Voronoi tessellations. *Numerical Mathematics* 3, 119–142. doi:10.4208/nmtma.2010.32s.1
- Figeac, N., Jagla, T., Aradhya, R., Da Ponte, J.P., Jagla, K., 2010. Drosophila adult muscle precursors form a network of interconnected cells and are specified by the rhomboid-triggered EGF pathway. *Development (Cambridge, England)* 137, 1965–1973. doi:10.1242/dev.049080
- Folker, E.S., Baylies, M.K., 2013. Nuclear positioning in muscle development and disease. *Front Physiol* 4, 363. doi:10.3389/fphys.2013.00363
- Gundersen, G.G., Worman, H.J., 2013. Nuclear Positioning. *Cell* 152, 1376–1389. doi:10.1016/j.cell.2013.02.031
- Gundersen, K., 2016. Muscle memory and a new cellular model for muscle atrophy and hypertrophy. *J. Exp. Biol.* 219, 235–242. doi:10.1242/jeb.124495
- H Keshishian, K Broadie, A Chiba, A., Bate, M., 2003. The Drosophila Neuromuscular Junction: A Model System for Studying Synaptic Development and Function. <http://dx.doi.org/10.1146/annurev.ne.19.030196.002553> 19, 545–575. doi:10.1146/annurev.ne.19.030196.002553
- Hall, Z.W., Ralston, E., 1989. Nuclear domains in muscle cells. *Cell* 59, 771–772. doi:10.1016/0092-8674(89)90597-7
- Jevtić, P., Levy, D.L., 2014. Mechanisms of nuclear size regulation in model systems and cancer. *Advances in experimental medicine and biology* 773, 537–569. doi:10.1007/978-1-4899-8032-8\_25
- Levy, D.L., Heald, R., 2012. Mechanisms of intracellular scaling. *Annual Review of Cell and Developmental Biology* 28, 113–135. doi:10.1146/annurev-cellbio-092910-154158
- Ma, T.-H., Lee, L.-W., Lee, C.-C., Yi, Y.-H., Chan, S.-P., Tan, B.C.-M., Lo, S.J., 2016. Genetic control of nucleolar size: An evolutionary perspective. *Nucleus* 7, 112–120. doi:10.1080/19491034.2016.1166322
- Manhart, A., Windner, S., Baylies, M., Mogilner, A., 2018. Mechanical positioning of multiple nuclei in muscle cells. *PLoS Comput Biol* 14, e1006208. doi:10.1371/journal.pcbi.1006208

- Metzger, T., Gache, V., Xu, M., Cadot, B., Folker, E.S., Richardson, B.E., Gomes, E.R., Baylies, M.K., 2012. MAP and kinesin-dependent nuclear positioning is required for skeletal muscle function. *Nature* 484, 120–124. doi:10.1038/nature10914
- Pavlath, G.K., Rich, K., Webster, S.G., Blau, H.M., 1989. Localization of muscle gene products in nuclear domains. *Nature* 337, 570–573. doi:10.1038/337570a0
- Piccirillo, R., Demontis, F., Perrimon, N., Goldberg, A.L., 2014. Mechanisms of muscle growth and atrophy in mammals and *Drosophila*. *Dev. Dyn.* 243, 201–215. doi:10.1002/dvdy.24036
- Pierce, S.B., Yost, C., Britton, J.S., Loo, L.W.M., Flynn, E.M., Edgar, B.A., Eisenman, R.N., 2004. dMyc is required for larval growth and endoreplication in *Drosophila*. *Development* (Cambridge, England) 131, 2317–2327. doi:10.1242/dev.01108
- Qaisar, R., Larsson, L., 2014. What determines myonuclear domain size? *Indian J. Physiol. Pharmacol.* 58, 1–12.
- Ranganayakulu, G., Elliott, D.A., Harvey, R.P., Olson, E.N., 1998. Divergent roles for NK-2 class homeobox genes in cardiogenesis in flies and mice. *Development* 125, 3037–3048. doi:10.1101/gad.7.7b.1325
- Roman, W., Gomes, E.R., 2017. Nuclear positioning in skeletal muscle. *Seminars in Cell & Developmental Biology*. doi:10.1016/j.semcdb.2017.11.005
- Rosser, B., Bandman, E., 2003. Heterogeneity of protein expression within muscle fibers. *American Society of Animal Science*. doi:10.2527/2003.8114\_suppl\_2E94x
- Schulman, V.K., Dobi, K.C., Baylies, M.K., 2015. Morphogenesis of the somatic musculature in *Drosophila melanogaster*. *Wiley interdisciplinary reviews. Developmental biology* 4, 313–334. doi:10.1002/wdev.180
- Team, R.C., 2013. R: A language and environment for statistical computing.
- Uppaluri, S., Weber, S.C., Brangwynne, C.P., 2016. Hierarchical Size Scaling during Multicellular Growth and Development. *Cell Reports* 17, 345–352. doi:10.1016/j.celrep.2016.09.007
- Van der Meer, S.F.T., Jaspers, R.T., Degens, H., 2011. Is the myonuclear domain size fixed? *Journal of musculoskeletal & neuronal interactions* 11, 286–297.
- Weber, S.C., Brangwynne, C.P., 2015. Inverse size scaling of the nucleolus by a concentration-dependent phase transition. *Curr. Biol.* 25, 641–646. doi:10.1016/j.cub.2015.01.012
- Whittaker, A.J., Royzman, I., Orr-Weaver, T.L., 2000. *Drosophila* double parked: a conserved, essential replication protein that colocalizes with the origin recognition complex and links DNA replication with mitosis and the down-regulation of S phase transcripts. *Genes & development* 14, 1765–1776.

**Figure 1.**

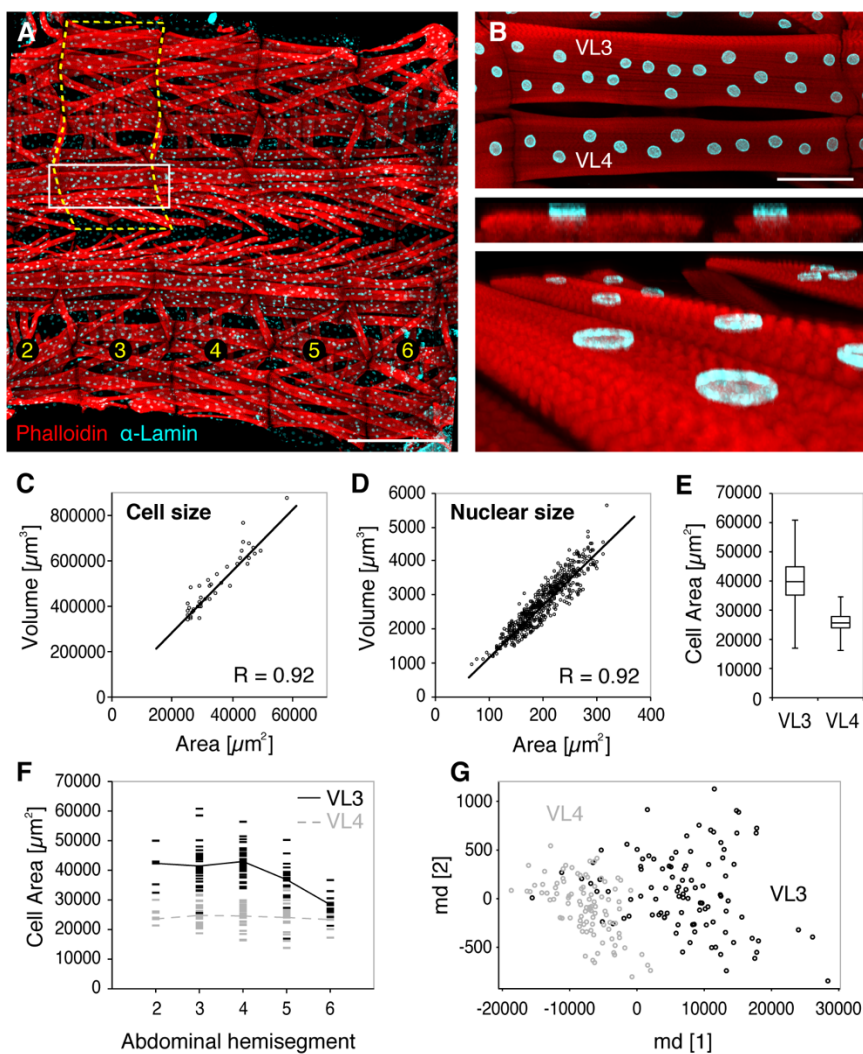


**Figure 1. Quantification of cell and nuclear sizes.**

(A) Flat prep of third instar *Drosophila* larva showing skeletal muscles (red, phalloidin) and nuclei (cyan,  $\alpha$ -Lamin) in bilateral abdominal hemisegments 2–6; anterior, left. Dashed line indicates one abdominal hemisegment; white box indicates Ventral Longitudinal (VL) muscles 3 and 4.

(B) Flattened confocal z-stack (top), optical cross sections (middle) and 3D rendering (bottom) of VL3 and VL4 muscles.

(C,D) Scatter plots comparing area and volume measurements for individual VL muscle cells (C) and nuclei (D). Linear regression curves and correlations coefficients ( $R$ ) are indicated.  $n$  (cells) = 42,  $n$  (nuclei) = 572

(E) Median VL3 and VL4 cell areas. Boxes, 25/75 percentiles; whiskers, min/max values.  $n_{VL3} = 102$ ,  $n_{VL4} = 97$ .  $p < 0.0001$  (Student's t test).

(F) VL3 (black) and VL4 (gray) muscle areas plotted over the corresponding muscle positions along the larvae. Lines represent mean values.  $n_{VL3} = 102$ ,  $n_{VL4} = 97$ .

(G) Unsupervised multidimensional cluster analysis of VL muscles from 3 different genetic control backgrounds ( $w^{1118}$ , *Dmef2-GAL4;UAS-2xEGFP*, *Dmef2-GAL4;UAS-GFP RNAi*, two experimental replicates each) using the following parameters: cell size, cell shape (aspect ratio), nuclear number, total nuclear area, axis level (abdominal hemisegment number). VL3 (black) and VL4 (gray) muscles form separate clusters with little overlap. See also Figure S1A.  $n_{VL3} = 102$ ,  $n_{VL4} = 97$ .

Scale bars, 500  $\mu\text{m}$  (A) and 100  $\mu\text{m}$  (B).

**Figure 2.**

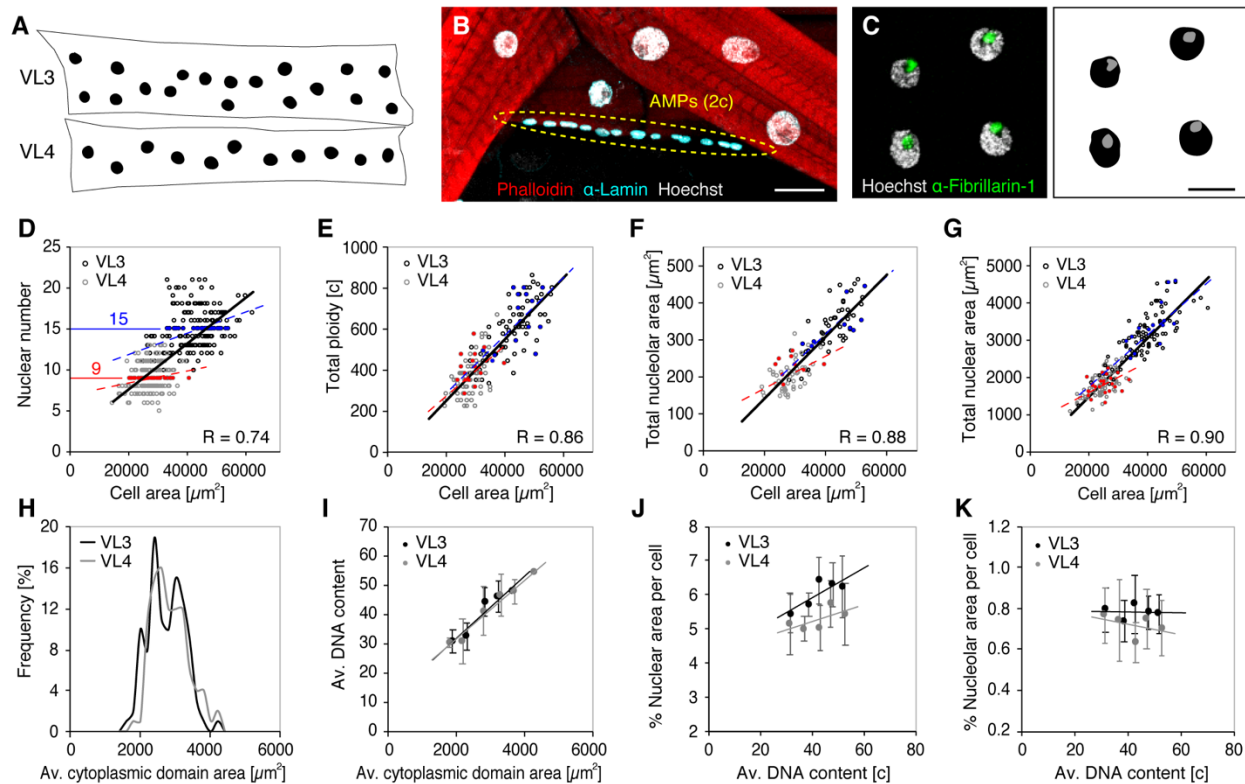


**Figure 2. Muscle nuclei establish precise global scaling with cell size.**

(A) Binary image of VL3 and VL4 muscles and nuclei shown in Figure 1B.

(B) Staining of DNA (Hoechst, gray) in diploid (2c) adult muscle progenitors (AMPs, dashed oval) and polyplloid VL muscle nuclei. Red, phalloidin; Cyan, Nucleus,  $\alpha$ -Lamin. See also Figures S1B-S1D.

(C) Left: labeling of nucleoli ( $\alpha$ -Fibrillarin, green) and DNA (Hoechst, gray) in VL muscle nuclei. Right: binary image for quantification.

(D-G) Nuclear number ( $n_{VL3}=102$ ,  $n_{VL4}=97$ ) (D), cumulative DNA copy number (c) (E) (total ploidy;  $n_{VL3}=67$ ,  $n_{VL4}=75$ ), cumulative nuclear area ( $n_{VL3}=102$ ,  $n_{VL4}=97$ ) (F), and cumulative nucleolar area ( $n_{VL3}=54$ ,  $n_{VL4}=54$ ) (G) plotted against muscle cell area. Bold lines and correlations coefficients (R) indicate linear scaling across VL3 (black) and VL4 (gray) muscles. Dashed lines indicate individual linear regressions for VL3 (blue) and VL4 (red) muscles. Cells with the same number of nuclei, e.g. 9 (red) and 15 (blue), achieve different cell sizes, and vary in their cumulative amount of nuclear DNA, nucleolar sizes and nuclear sizes.

(H-K) Global size parameters as in (D-G) normalized by the number of nuclei per cell. Error bars, SD.VL3 (black) and VL4 (gray).

(H) Histogram showing mean cytoplasmic domain sizes (cell area/nuclear number) in VL3 and VL4 muscles.

(I) Mean DNA content (cumulative DNA content/nuclear number) plotted over the mean cytoplasmic domain size.

(J) Global nuclear scaling (% nuclear area per cell area) plotted over mean DNA content.

(K) Global nucleolar scaling (% nucleolar area per cell area) plotted over mean DNA content.

Scale bars,  $25\mu\text{m}$  (B,C).

**Figure 3.**

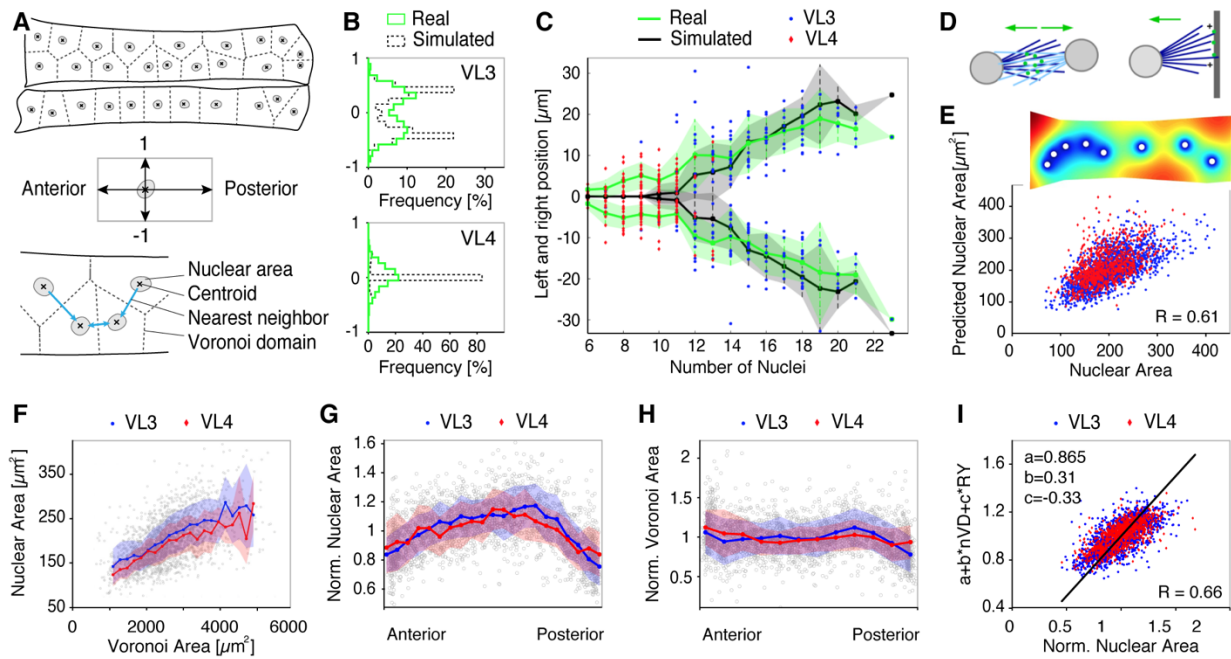


**Figure 3. Nuclear positioning regulates individual nuclear sizes**

(A) Schematic representation of VL3 and VL4 muscles and nuclei, nuclear centroids, nearest neighbor distances (blue arrows, bottom) and cytoplasmic domain sizes (Voronoi tessellation, dashed lines).

(B) Histograms of relative nuclear positions along the short cell axis. Real data (green lines) and simulated nuclear positions (dashed lines) show organization in one or two rows for each muscle type. For simulation details see methods.

(C) Nuclear position as a function of nuclear number. For each cell the average position of all nuclei to either side of the cell midline was plotted (experimental data in green, simulated data in black). Thick lines and shaded regions show means, SD; each dot represents one cell (VL3 blue, VL4, red).

(D) Schematic representation of simulated mechanical forces between neighboring nuclei (left) and between nuclei and cell edges (right) (after (Manhart et al., 2018)).

(E) Scatter plot showing correlation of real nuclear areas with nuclear areas predicted by simulation of local size sensing. For simulation details see methods. Inset (top) shows representative simulation result; colors indicate concentration of a hypothetical cytoplasmic molecule which is absorbed by each nucleus (white circles).

(F-H) Thick lines and shaded regions show means, SD; each dot represents one cell (VL3 blue, VL4, red).

(F) Linear correlation of nuclear areas with Voronoi domain areas ( $R=0.55$ ,  $p<0.0001$ ).

(G) Distribution of normalized nuclear areas (Nuclear Area\*No. of Nuclei/Total Nuclear Area) along the cells showing largest nuclei in the cell middle. VL3 nuclei (mean $\pm$ SD = 202 $\pm$ 55 $\mu\text{m}$ ) are larger than in VL4 nuclei (192 $\pm$ 44 $\mu\text{m}$ ).

(H) Distribution of normalized Voronoi domain size (Voronoi Area\*No. of Nuclei/Cell Area) along the cell length. Thick lines show averages, shaded regions correspond to standard deviation.

(I) Multiple Linear Regression showing that Voronoi area (nVD=normalized Voronoi Area) and nuclear position along the long cell axis (RY=absolute relative y-position, with 0=middle and 1=poles) give a good prediction of nuclear size ( $R=0.66$ ,  $p<0.0001$ ). Each dot represents one cell (VL3 blue, VL4, red).

n (cells) = 200 (103 VL3, 97 VL4), n (nuclei) = 2477 (1579 VL3, 898 VL4).

**Figure 4.**

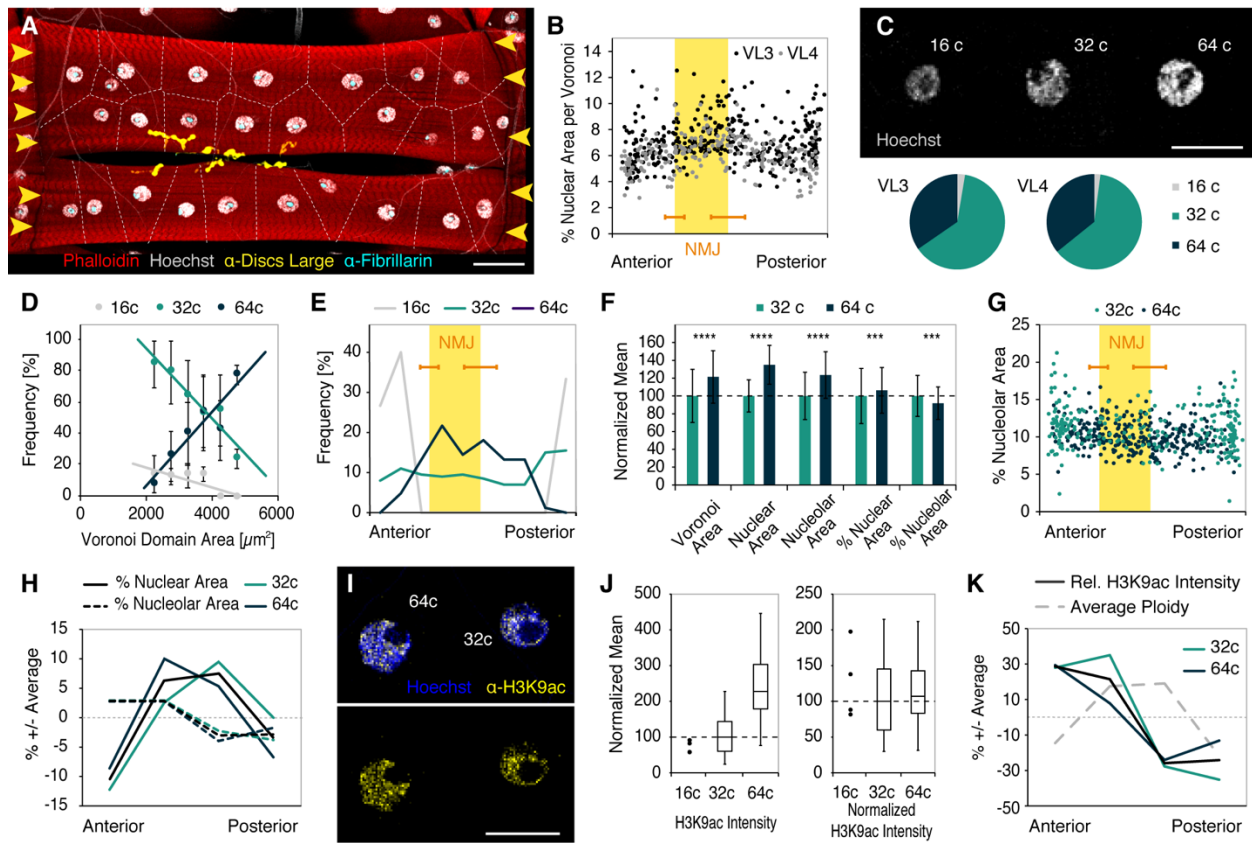


**Figure 4. Local nuclear size scaling and synthetic activity are inversely correlated.**

- (A) Positions of NMJ ( $\alpha$ -Discs large, yellow) and MTJs (yellow arrowheads) in VL3 and VL4 muscles. Muscle, Red, phalloidin; nuclei, white, Hoechst; nucleolus, cyan,  $\alpha$ -Fibrillarin.
- (B) Scatter plot showing local nuclear size scaling (% nuclear area per Voronoi domain) along the length of VL muscle fibers ( $n_{VL3}=24$ ,  $n_{VL4}=24$  muscles). Highest values correlate with mean position of the NMJ (yellow; start:  $29.03\pm 4.48\%$ , end:  $53.74\pm 7.88\%$  of cell length).  $n_{VL3}=24$ ,  $n_{VL4}=24$ . Error bars, SD.
- (C) VL muscles nuclei containing 16, 32 or 64 copies (c) of DNA (top). The ratio of nuclear ploidies is similar in VL3 and VL4 muscles (pie charts, bottom; 16c, gray; 32c, green, 64c, black here and in panels D-H, K). See also Figure S1.
- (D) Frequency of 16c, 32c and 64c nuclei as a function of mean Voronoi domain size. The ratio of nuclear ploidy numbers in individual cells depends on nuclear number and cell size.
- (E) Histogram of nuclear ploidy numbers along the long cell axis (anterior left, posterior right). NMJ region noted by yellow box; orange error bars, SD?
- (F) Bar graph (mean  $\pm$  SD) comparing absolute size of Voronoi domain ( $p<0.0001$ ), nuclear area ( $p<0.0001$ ) and nucleolar area ( $p<0.0001$ ), and size scaling (% nuclear area per Voronoi domain,  $p=0.0009$ ; % nucleolar per nuclear area,  $p<0.0001$ ) in nuclei with 32 and 64 copies of nuclear DNA. Means for 32c nuclei were set to 100%.

(G) Nucleolar size scaling (% nuclear area per nuclear area) along the length of VL muscle fibers. NMJ position (as in (A)) is indicated in yellow orange error bars, SD?.

(H) Size scaling of nuclei (% nuclear area) and nucleoli (% nucleolar area) shows inverse behavior along the length of each muscle fiber, independent of absolute DNA content.

(I) Representative images showing expression of H3K9ac (yellow) and DNA (Hoechst, blue) in polyploid VL nuclei.

(J) Box plots (median, 25/75 percentile, min/max values) showing proportional increase of H3K9ac with DNA content yet similar relative values per nucleus, independent of absolute DNA content.

(K) Along each muscle fiber, 32c and 64c nuclei show higher relative H3K9ac levels in the anterior than in the posterior of cells. Dashed line indicates average nuclear ploidy along the cells.

Scale bars:  $50 \mu\text{m}$  (A),  $25 \mu\text{m}$  (C,I).

Sample numbers: n=905 nuclei (C-F); b, g, h, n=577 nuclei (B,G,H), n= 240 nuclei (J,K).

**Figure 5.**

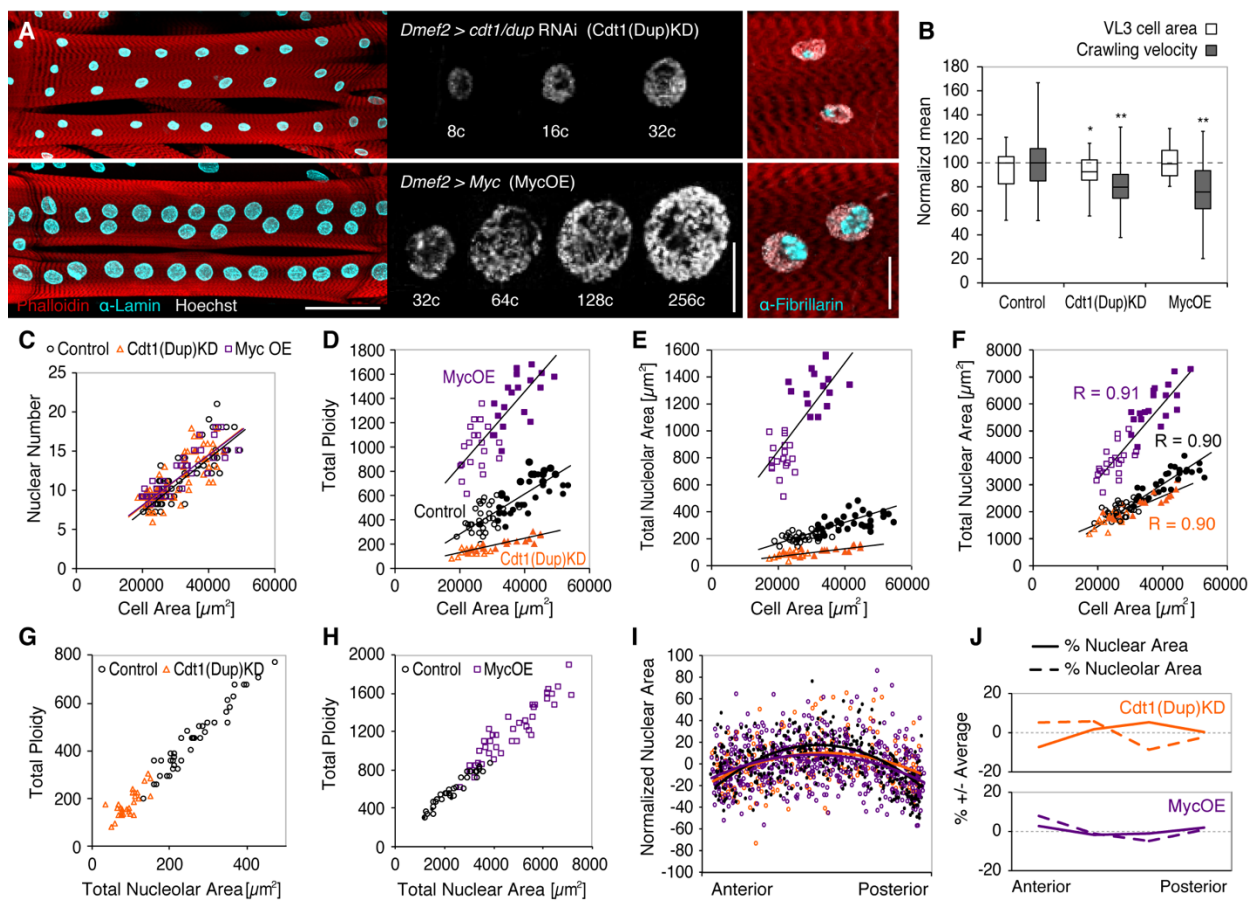


**Figure 5. Muscle specific manipulations of nuclear DNA content.**

(A) VL3 and VL4 with muscle-specific knockdown of Cdt1(Dup) (top) and overexpression of Myc (bottom). For representative control image see Figure 1B. Changes in nuclear DNA content (Hoechst, gray) and nucleolar sizes ( $\alpha$ -Fibrillarin, cyan) are shown in panels in the middle and on the right, respectively. Muscle, phalloidin, red; nuclei,  $\alpha$ -Lamin, cyan (left panel).

(B) Boxplot showing median VL3 cell areas and larval crawling velocities in Cdt1(Dup)KD, MycOE, and control larvae (boxes, 25/75 percentiles; whiskers, min/max values). Cell areas are only slightly reduced in Cdt1(Dup)KD (n=39 cells, p=0.1714) and unchanged in MycOE (n=18 cells, p=0.5760) when compared to control (n=28 cells). Larval crawling velocity is significantly reduced in Cdt1(Dup)KD (n=24 larvae, p=0.0044) as well as in MycOE (n=27 larvae, p=0.0017) compared to control (n=27 larvae). p values and asterisks indicate Student's t test results.

(C-F) Scatter plots showing scaling of nuclear number(C), cumulative DNA content(D), cumulative nucleolar area(E) and nuclear area(F) across VL 3 (filled symbols) and VL4 muscle types (outlined symbols) in Cdt1(Dup)KD (orange), MycOE (purple) and control muscles (black).

(G) Linear isometric scaling of cumulative nucleolar area with DNA content in Cdt1(Dup)KD muscles.

(H) Linear isometric scaling of cumulative nuclear area with DNA content in MycOE muscles.

(I) Distribution of nuclear areas along the length of each muscle fibers. Values are expressed as % deviation from average per genotype. Solid lines indicate mean. The distribution of nuclear areas in the Cdt1(Dup)KD and in MycOE is similar to control.

(J) Nuclear size scaling (% nuclear area per Voronoi domain, solid lines) and nucleolar size scaling (% nucleolar area per nucleus, dashed line) along the length of Cdt1(Dup)KD (orange) and MycOE (purple) muscles.

Scale bars: **a**, 100  $\mu$ m (left), 25  $\mu$ m (middle, right).

Sample numbers: Control,  $n_{VL3}=28$ ,  $n_{VL4}=35$  cells; Cdt1(Dup)KD,  $n_{VL3}=39$ ,  $n_{VL4}=35$  cells; MycOE,  $n_{VL3}=18$ ,  $n_{VL4}=19$  cells (C-J).

**Figure 6.**

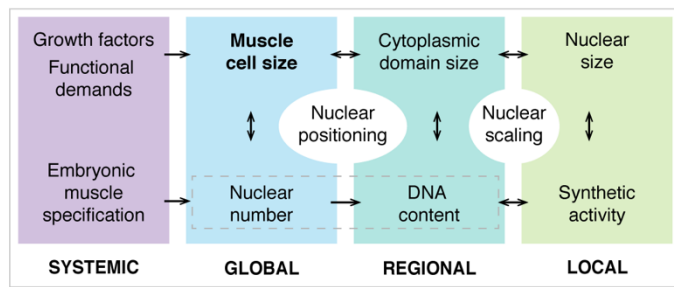


**Figure 6. Levels of intracellular size regulation in multinucleated muscle fibers.**

## **STAR Methods**

### **CONTACT FOR REAGENT AND RESOURCE SHARING**

Further information and request for resources and reagents should be directed to and will be fulfilled by the Lead Contact Mary K. Baylies ([m-baylies@ski.mskcc.org](mailto:m-baylies@ski.mskcc.org)).

### **EXPERIMENTAL MODEL AND SUBJECT DETAILS**

#### **Fly stocks and staging**

The following *Drosophila* stocks were maintained under standard conditions on cornmeal medium: *w<sup>1118</sup>* (Bloomington 3605), *Dmef2-GAL4* (Ranganayakulu et al., 1998), *UAS-2xEGFP* (Bloomington 6874), *UAS-GFP RNAi* (from J. Zallen, SKI), *UAS-dmyc* (from N. Perrimon), *UAS-dup (double parked/Ctd1) RNAi* (from T. Orr-Weaver). Crosses (GAL4 X UAS) were performed at 25 °C on apple juice plates. For all experiments, embryos hatched within a 2h period were selected and raised to third instar larval stage on cornmeal medium at 25 °C.

### **METHOD DETAILS**

#### **Dissections, labeling and confocal imaging**

Wandering third instar larvae were dissected, fixed in 10% formalin and labeled as previously described (Metzger et al., 2012). Muscle cells were labeled using Alexa Fluor-conjugated phalloidin (Life Technologies). Anti-Lamin (ADL67.10, DSHB; 1:100), anti-Fibrillarin (MCA-38F3, EnCor; 1:100), anti-H3K9ac (Active Motif; 1:200), anti-discs large (4F3, DSHB; 1:200), anti-alpha tubulin (Sigma, 1:500) primary antibodies and Alexa Flour-conjugated secondary antibodies (Life Technologies; 1:200) were used to label cellular and nuclear structures. Hoechst 33342 (Invitrogen; 1 µg/ml) was used to label nuclear DNA. Whole larvae were mounted in ProlongGold (Invitrogen). VL3 and VL4 muscles in abdominal hemisegments 2-6 were imaged on a LSM 700 confocal microscope (Zeiss). All samples intended for direct comparison were imaged using the same confocal settings.

#### **Image processing and measurements**

All images were processed and analyzed using standard ImageJ measurement tools. For 2D quantification of VL3 and VL4 muscles, z-projections of confocal images were used. VL3 and

VL4 cell areas were traced by hand, based on phalloidin labeling. Outlines were used to record shapes (aspect ratio; cell width/cell length), sizes (areas) and positions (coordinates) of individual cells. Automated thresholding of fluorescence intensities of anti-Lamin and/or Hoechst labeling was used to generate binary images of VL nuclei. We recorded the number, size (areas) and position (centroids) of all nuclei within each cell, and we used the binary images as masks to measure Hoechst and H3K9ac fluorescence intensities (sum intensity of pixel density) within those nuclei. Further, nuclear centroids were used to calculate nearest neighbor distances and perform Voronoi tessellation (Du et al., 2010). Automated thresholding of anti-Fibrillarin labeling was used to generate binary images of nucleoli and measure nucleolar sizes (areas). For calculation of DNA content, we normalized Hoechst fluorescence intensities of each muscle nucleus to diploid Adult Muscle Progenitors (AMPs) (Figeac et al., 2010) from the same larva. To determine NMJ length, we generated binary imaged of anti-discs large labeling and recorded area and position of the NMJ in relation to VL3 and VL4 cells.

For 3D measurements of VL cell and nuclei, we determined the average depth/thickness of each cell and of all nuclei from one representative experiment. Volumes were calculated by multiplying thickness values with area measurements.

### **Simulation of random nuclear positioning**

To simulate random positioning of nuclei within VL muscle fibers, we used actual cell parameters of 200 wild-type cells (width, height, number of nuclei) and positioned nuclei randomly following uniform distributions. To assess the influence of stochasticity on our results, we repeated this procedure 1000 times. We calculated mean nearest neighbor distances and standard deviations for VL3 and VL4 nuclei.  $\pm$  std. The fits of Gaussians to the data (thick lines) were computed using the measured mean and std of the data.

### **Simulation of nuclear positioning**

We simulated the positioning of N equally sized nuclei in a rectangular domain that interact with each other and with the cell sides via an isotropic pushing force, decreasing with distance. To underscore the differences between VL3 and VL4 cells, only cells from hemisegments 1-4 were used. Since we are working in a low Reynolds number regime, we can assume a friction-dominated environment, i.e. the velocities of the nuclei are proportional to the forces acting on them. Since

we are only interested in equilibrium positions, we can rescale in order to normalize the coefficient of the internuclear interactions to 1. We assume the position of the centroid of the i-th nucleus follows

$$\frac{d}{dt}X_i(t) = \sum_{j=1, j \neq i}^N f(d_{ij})N_{ij} + \sum_{k=L,R,U,D}^N q f(d_{ik})N_{ik}$$

where  $d_{ij}$  is the distance between centroids i and j,  $N_{ij}$  is the vector of length 1 pointing from nucleus j to nucleus i. For the interactions with the sides, we define  $d_{ik}$  as the shortest distance between the i-th nucleus and the side with index k (L=left, R=right, U=upper, D=down) and  $N_{ik}$  is the unit vector normal to that side pointing towards the i-th nucleus. The scalar function  $f(d) > 0$  is a distance dependent pushing force and q is a free parameter describing the ratio between internuclear and nucleus-side forces. We used  $f(d) = 1/d$  and  $f(d) = 1/d^2$ . To directly compare with the data, we used the same cell widths, heights and number of nuclei as measured for the experimental data. As initial conditions the real positions were used, since this allows the use of the mean distance between the real and final (equilibrium) positions of the nuclei as an error functional in the simulation. This error was minimized with respect to q. Here only the results using  $f(d) = 1/d^2$  are shown, which gave a better fit with the data. The error functional was minimal for  $q=0.7$ . To simulate, we used Matlab's ode solver *ode15*, a variable-step, variable-order solver.

### Simulation of space-sensing

We simulated the distribution of a signaling molecule, that is produced at a constant rate everywhere in the cell and diffuses until it is absorbed by a nucleus. For each cell, the real geometry and nuclear positions were used with nuclear radii of  $3.8\mu\text{m}$ . Mathematically, we solve the Poisson equation in 2D within each cell using Neumann boundary conditions at the cell membrane and Dirichlet boundary conditions at the nuclear envelope, i.e. if  $s(x)$  is the concentration of the signal at position  $x$ , we solve

$$\begin{aligned}\Delta s &= -1, x \in C \\ s &= 0, x \in \partial N \\ \nabla s \cdot n &= 0, x \in \partial C\end{aligned}$$

where  $\partial N$  denotes the union of all the boundaries of all nuclei and  $\partial C$  is the cell boundary. We solve using a Finite Element Method with an adaptive mesh utilizing Matlab's PDE toolbox. The amount

of signal each nucleus receives,  $S$ , was calculated as the integral of the fluxes at its boundary. We assumed a linear relationship between the amount of signal received and the area of the nucleus  $A$ :

$$A = A_{min} + \alpha S$$

We fitted the parameters  $A_{min}$  (the minimal nuclear area) and  $\alpha$  (the sensitivity) to maximize the correlation between simulated and measured nuclear sizes, yielding  $A_{min}=83 \mu\text{m}^2$  and  $\alpha=0.044 \mu\text{m}^2$  per unit signal.

### **Larval locomotion assay**

Third instar larvae were placed in the center of a 10 cm apple juice plate (stained with green food color for better contrast) and recorded for 1 minute using an iPhone SE (Apple) on a custom mount. Each genotype was analyzed in 2 independent experiments; per individual experiment, a minimum of 10 larvae was analyzed. Movies of larval locomotion were processed and quantified in ImageJ using the trackmate plugin. Average velocities (+/- standard deviation) per genotype.

## **QUANTIFICATION AND STATISTICAL ANALYSIS**

Sample sizes were chosen based on previous experience in the laboratory. Each experiment was performed in 2 technical replicas; per individual experiment a minimum of 4 larvae (biological replicates) and at least 8 VL muscles per larva were analyzed. For wildtype analyses we quantified a total of 102 VL3 and 97 VL4 muscles from three control genotypes ( $w^{1118}$ ,  $Dmef2-GAL4;UAS-2xEGFP$ ,  $Dmef2-GAL4;UAS-GFP RNAi$ ). Two-tailed Student's  $t$ -test and correlation coefficients (R) were computed using GraphPad Prism version 7.0a for Mac (GraphPad Software).

### **Unsupervised multidimensional cluster analysis**

Analysis was performed in R statistical language ((Team, 2013). Data was clustered using classical multidimensional scaling (MDS) using cmdscale() function with Euclidean distances and default parameters.

### **Multiple linear regression analysis**

To allow for direct comparison of the data and assess which parameters best predict nuclear sizes, we normalized all parameters (see below). The best prediction gave the following linear regression model: normalized (norm.) nuclear area =  $a + b$  (norm. Voronoi area) +  $c$  (norm. distance to center). Where norm. nuclear area = nuclear area divided by the mean nuclear area in each cell; norm. Voronoi area = Voronoi area divided by the mean Voronoi area in each cell; norm. distance to center is defined between 0 (center) and 1 (poles). We fitted coefficients  $a,b,c$  of the linear regression model, yielding  $a=0.87$ ,  $b=0.31$ ,  $c=-0.33$ . p-values are well below 1% for both variables.  $R^2=0.477$ . Note that norm. Voronoi area and norm. distance to center are not correlated with each other ( $R=-0.082$ ).

## KEY RESOURCES TABLE

REAGENT or RESOURCE	SOURCE	IDENTIFIER
<b>Antibodies</b>		
Mouse anti-Lamin	DHSB	ADL67.10
Mouse anti-Fibrillarin1	EnCore	MCA-38F3
Rabbit anti-H3K9ac	Active Motif	Catalog No: 39138
Mouse anti-Discs Large	DHSB	4F3
Mouse anti-alpha tubulin	Sigma	DM1A
Goat anti-mouse Alexa conjugated secondaries	Life Technologies	
<b>Experimental Models: Organisms/Strains</b>		
<i>D. melanogaster</i> : w1118	Bloomington Drosophila Stock Center	BDSC:3605
<i>D. melanogaster</i> : Dmef2-Gal4	(Ranganayakulu et al., 1998)	
<i>D. melanogaster</i> : UAS-2xEGFP	Bloomington Drosophila Stock Center	BDSC:6874
<i>D. melanogaster</i> : UAS-GFP RNAi	from J. Zallen (SKI)	
<i>D. melanogaster</i> : UAS-dmyc	from N. Perrimon	
<i>D. melanogaster</i> : UAS-dup (double parked/Cdt1) RNAi	from T. Orr-Weaver	
<b>Software and Algorithms</b>		
ImageJ/Fiji	Fiji	<a href="https://fiji.sc/">https://fiji.sc/</a>
GraphPad Prism	GraphPad	<a href="https://www.graphpad.com/">https://www.graphpad.com/</a>
Excel	Microsoft	<a href="https://products.office.com/en-us/excel">https://products.office.com/en-us/excel</a>
Matlab	Mathworks	<a href="https://www.mathworks.com/products/matlab.html">https://www.mathworks.com/products/matlab.html</a>
Imaris	Bitplane	<a href="http://www.bitplane.com/imiris/imiris">http://www.bitplane.com/imiris/imiris</a>
R	R Foundation for Statistical Computing	<a href="https://www.r-project.org/">https://www.r-project.org/</a>
Cytosim	Nédélec Laboratory	<a href="http://github.com/nedelec/cytosim">http://github.com/nedelec/cytosim</a>
Illustrator	Adobe	<a href="http://www.adobe.com">www.adobe.com</a>

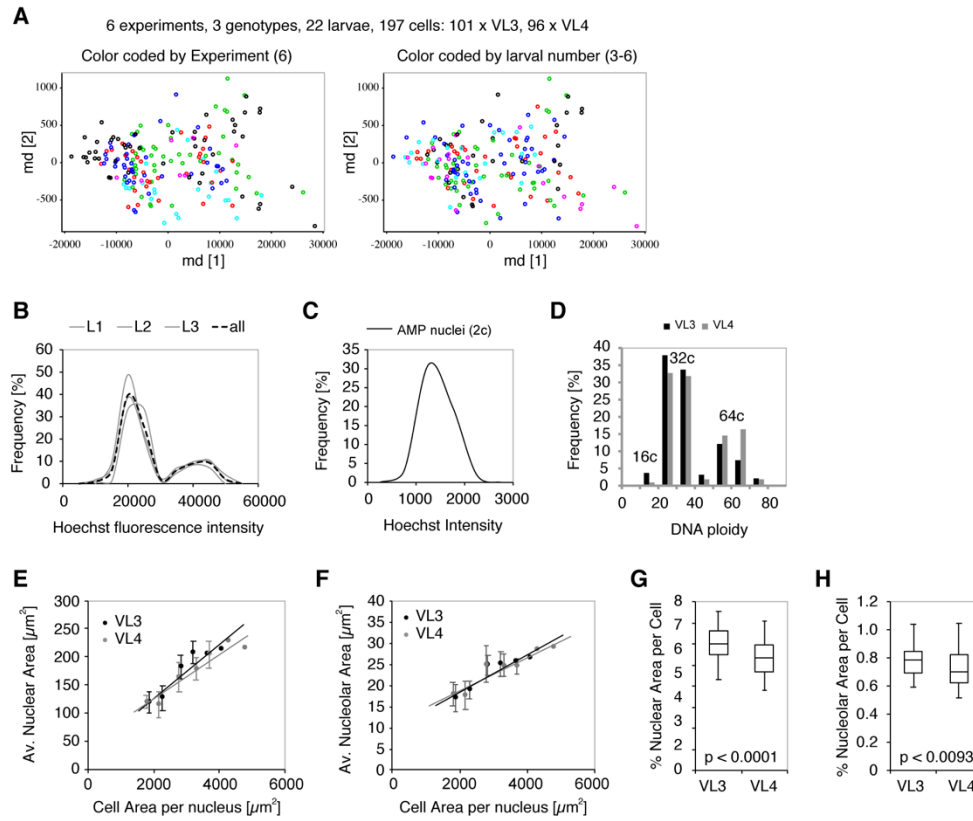


**Figure S1. Muscle nuclei establish precise global scaling with cell size. Related to Figures 1 and 2.**

(A) Unsupervised multidimensional cluster analysis of VL muscles from 3 different genetic control backgrounds ( $w^{1118}$ , *Dmef2-GAL4;UAS-2xEGFP*, *Dmef2-GAL4;UAS-GFP RNAi*, two experimental replicates each) using the following parameters: cell size, cell shape (aspect ratio), nuclear number, total nuclear area, axis level (abdominal hemisegment number). Cells cluster in 2 groups, which clearly correspond to the VL3 and VL4 muscles (Figure 1G) but show no bias for experimental replicate (left) or individual larvae (right).  $n_{VL3} = 102$ ,  $n_{VL4} = 97$ .

(B) Histogram of DNA (Hoechst) fluorescence intensities in individual VL muscle nuclei from 3 individual larvae (L1-L3, gray). VL nuclei per larva  $n \geq 100$ . Black dashed line represents mean values.

(C) Histogram of Hoechst intensities in diploid (2c) adult muscle progenitors (AMPs).  $n = 90$ .

(D) Histogram of calculated DNA copy numbers (ploidy) for nuclei plotted in (B). Peaks correspond to nuclei containing 16, 32 or 64 copies (c) of DNA.

(E,F) Mean nuclear(E) and mean nucleolar areas(F) plotted over mean cytoplasmic domain area ( $n_{VL3}=54$ ,  $n_{VL4}=54$ ).

(G,H) Boxplots comparing global nuclear scaling (G) (% nuclear area per cell, see also (E)) and global nucleolar scaling (H) (% nucleolar area per cell, see also (F)) in VL3 and VL4 muscles. Medians, 27/75 percentiles, min/max values. Both scaling parameters are significantly lower in VL4 muscles (p values indicate Student's t test result).

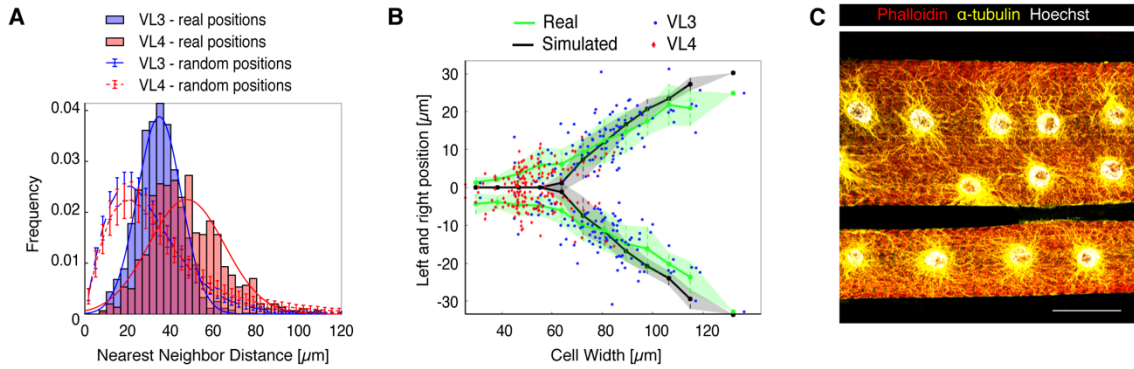


**Figure S2. Nuclear positioning regulates individual nuclear sizes. Related to Figure 3.**

(A) Histogram of Nearest Neighbor Distances (NNDs) in VL3 (blue) and VL4 (red) in comparison to random distribution of nuclei (for simulation details see methods). NNDs follow normal distributions (blue and red lines) with mean  $\pm$  SD:  $34.8 \pm 10.3$  and  $47.6 \pm 17.7$  for VL3 and VL4 muscles, respectively.

(B) Nuclear position as a function of cell width. For each cell, the average position of all nuclei to the left and right of the cell midline was determined (experimental data in green, simulated data in black). Thick lines and shaded regions show the mean and mean  $\pm$  standard deviation, each dot represents one cell (VL3 blue, VL4, red). As cell width increases, nuclei move from the cell midline to the sides. This behavior is consistent across VL3 and VL4 muscles and predicted by the simulations. Sample numbers: 200 cells (103 VL3, 97 VL4), 2477 nuclei (1579 VL3, 898 VL4).

(C) VL3 and VL4 muscles labeled with phalloidin (red) and anti- $\alpha$ -tubulin (yellow) antibodies. Nuclear DNA (Hoechst) is shown in white. Scale bar: 50  $\mu\text{m}$ .

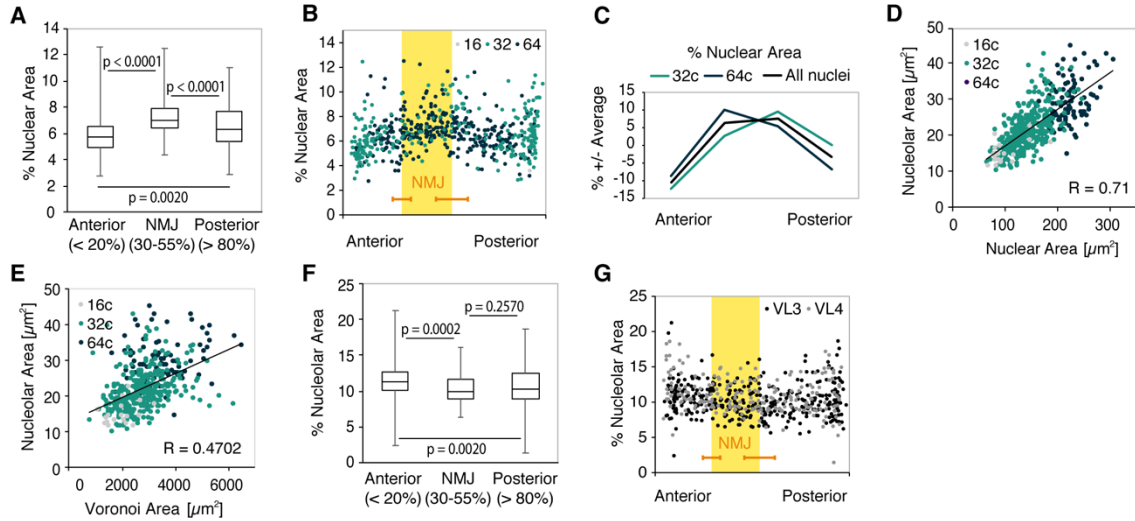


**Figure S3. Coordination of nuclear size scaling and synthetic activity. Related to Figure 4.**

(A) Box plot comparing median nuclear size scaling (% nuclear area per Voronoi domain) at the anterior and posterior MTJs (20% of cell length) and the NMJ (30-55% of cell length). p values indicate Student's t test result.

(B) Scatter plot showing nuclear size scaling along the long cell axis of VL3 and VL4 muscles. Position of the NMJ is indicated in yellow (start: 29.03+/-4.48%, end: 53.74+/-7.88% of cell length; orange bars: mean +/- standard deviation). Color of dots indicate the copy number of individual nuclei.

(C) Normalized nuclear size scaling associated with nuclei containing 32 or 64 copies of DNA along the muscle fibers.

(D,E) Scatter plots demonstrating local scaling of nucleolar areas with nuclear areas (D)(R=0.71) and with Voronoi domain areas (E) (R=0.47). Color of dots indicate the copy number of individual nuclei.

(F) Box plot comparing median nucleolar size scaling (% nucleolar area per nuclear area) at the anterior and posterior MTJs (20% of cell length) and the NMJ (30-55% of cell length). p values indicate Student's t test result.

(G) Nucleolar size scaling (% nucleolar area per nucleus) plotted against the long cell axis. VL3 and VL4 nuclei and position of the NMJ are indicated as in (B). Black dots: VL3, grey dots: VL4.

Sample numbers: n=905 nuclei (C-F); b, g, h, n=577 nuclei (B,G,H), n= 240 nuclei (J,K).

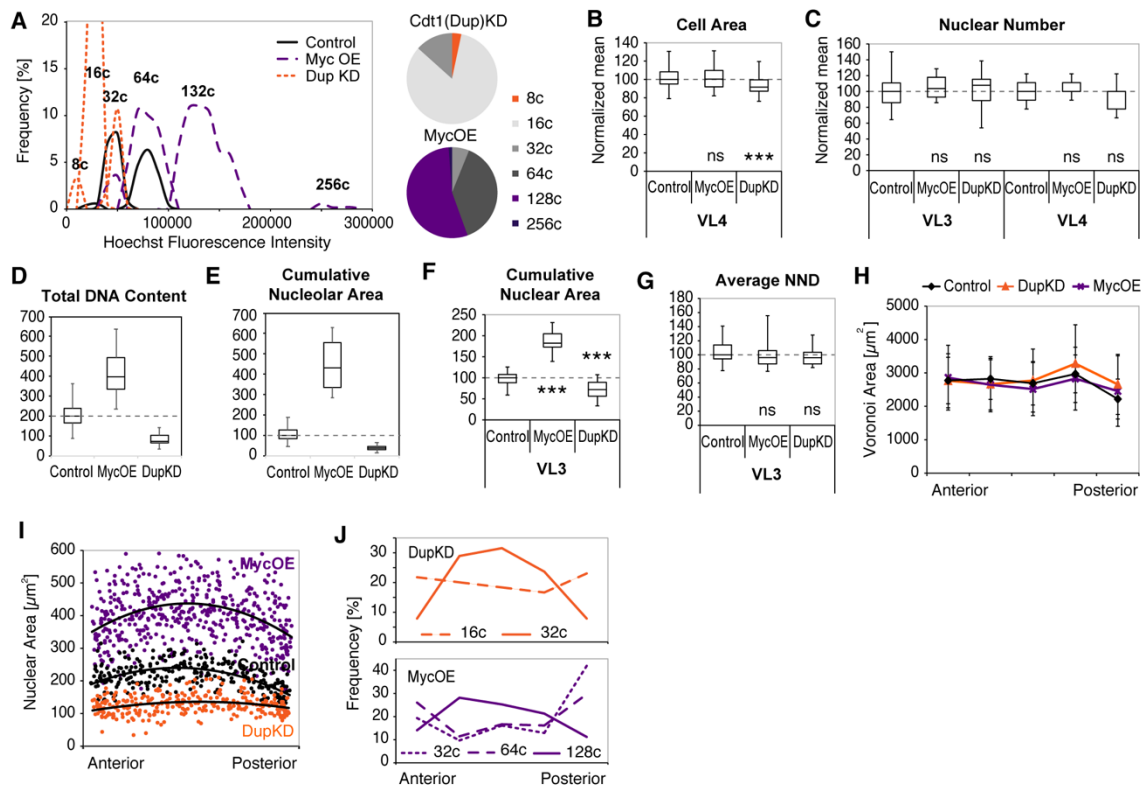


**Figure S4. Muscle specific manipulations of nuclear DNA content. Related to Figure 5.**

(A) Left: Histogram of DNA (Hoechst) fluorescence intensities showing decreased nuclear DNA content in Cdt1(Dup)KD ( $n_{VL}=25$ ,  $n_{VL4}=24$ ) and DNA increased DNA content in Myc OE muscles ( $n_{VL}=21$ ,  $n_{VL4}=19$ ). Right: Pie charts of nuclear ploidies in Cdt1(Dup)KD ( $n_{VL}=25$ ,  $n_{VL4}=24$ ) and MycOE muscles. Ploidy classes not found in control muscles are highlighted in orange (8c; Cdt1(Dup)KD) and purple (128c, 256c; MycOE).

(B,C) Box plots (whisker, min/max values; boxes, 25/75 percentiles) comparing median cell areas(B) and nuclear numbers(C) in Cdt1(Dup)KD, Myc OE and control muscles (dashed line indicates median). Student's t test results: (B) MycOE,  $p=0.1268$ , Cdt1(Dup)KD,  $p=0.1269$ , (C) MycOE:  $p_{VL}=0.9959$ ,  $p_{VL4}=0.3720$ , Cdt1(Dup)KD:  $p_{VL}=0.0268$ ,  $p_{VL4}=0.0002$ .

(D-G) Boxplots (whisker, min/max values; boxes, 25/75 percentiles) showing median cumulative DNA content, nucleolar area, nuclear area and nearest neighbor distance (NND) in VL3 muscles of Cdt1(Dup)KD, Myc OE and control larvae. Student's t test results are  $p < 0.0001$  for both genotypes in (D,E,F),  $p = 0.1638$  (MycOE) and  $p = 0.5448$  (Cdt1(Dup)KD) in (G).

(H) Voronoi domain areas along the long cell axis (mean +/- SD). Colored lines indicate genotype.

(I) Scatter plots showing distribution of nuclear areas along the long cell axis.

(J) Histograms showing distribution of nuclear ploidies in Myc OE (h) and Cdt1(Dup)KD (i) muscles.

Sample numbers: Control,  $n_{VL}=28$ ,  $n_{VL4}=35$  cells; Cdt1(Dup)KD,  $n_{VL}=39$ ,  $n_{VL4}=35$  cells; MycOE,  $n_{VL}=18$ ,  $n_{VL4}=19$  cells.

# Cell size and nuclear scaling relationships in multinucleated muscle fibers - Mathematical Supplement

S. Windner, A. Manhart, A. Brown, A. Mogilner, M. Baylies

## 1 Space-sensing Model Details

Here, we provide details on the space-sensing model presented in the main text. In short, we suggest a mechanism which allows nuclei to sense the size of the space around them and adjust their size accordingly. The shape of larval muscle cells VL3 and VL4 is roughly a cuboid with typical dimensions

$$\text{width} \times \text{length} \times \text{depth} = 70\mu\text{m} \times 500\mu\text{m} \times 13\mu\text{m},$$

i.e. the cells are very flat. Nuclei have the shape of flat cylinders, or discs, all positioned on one of the broad cuboids faces. We start by describing the 2D model, in which we neglect the cells' depths; the 3D variant of the model is described below. We hypothesize that a signal molecule, with concentration  $s(x, y, t)$  at position  $(x, y)$  and time  $t > 0$ , is produced randomly anywhere in the cell with a constant rate  $\gamma$ . We also hypothesize that the signal molecules diffuse with diffusion constant  $D$ . If a molecule encounters a nucleus, it is absorbed by the nucleus. At each time instant the nucleus adjusts its size,  $A$  according the total amount of signal it receives. The nuclear size,  $A$ , denotes the 2D area of the disc shaped nucleus, however since the nuclei are very flat and their depth was not observed to be variable, the nuclear area is proportional to its volume.

To explore this model mathematically, we formulate the following system of differential equations:

$$\partial_t s = D\Delta s + \gamma \quad (x, y) \in \mathcal{C}, \tag{1}$$

$$\nabla s \cdot n = 0 \quad (x, y) \in \partial\mathcal{C},$$

$$s = 0 \quad (x, y) \in \bigcup_{i=1}^N \partial\mathcal{N}_i. \tag{2}$$

Here  $\mathcal{C}$  denotes the 2D cell excluding the space occupied by the nuclei and  $\partial\mathcal{C}$  is the outer boundary. The vector  $n$  is the outward unit normal along this boundary. The nuclei are indexed with  $i = 1, \dots, N$  and  $\partial\mathcal{N}_i$  is the boundary of the  $i$ -th nucleus. The first and second terms in the right hand side of the first equation describe the signal molecule diffusion and activation (or synthesis) with rate  $\gamma$ , respectively. The second equation is the no

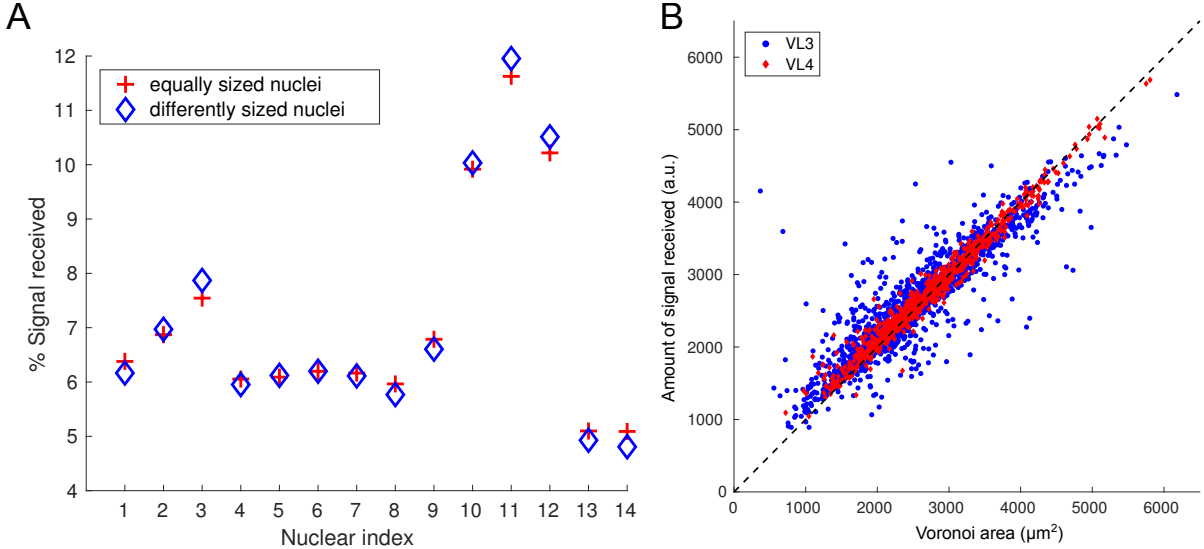


Figure M1: *A:* For the example cell shown in Fig. M2, we compared the % of the total amount of absorbed signal received by each nucleus if we solve (5) for equally sized nuclei ( $45\mu\text{m}^2$ ), or having different sizes (using the measured nuclear areas). As can be seen, the difference is less than 0.5%. *B:* Comparing the geometrically determined Voronoi areas with the amount of signal received, calculated by using (5) and (3).

flux boundary condition at the cell boundaries, and the third equation is the absorption boundary condition at the circular nuclear boundaries.

The amount of signal the  $i$ -th nucleus receives per unit time is given by the curve integral:

$$S_i = -D \int_{\partial N_i} \nabla s \cdot n \, d\Gamma_i, \quad (3)$$

where  $n$  is the unit normal pointing from the cell towards the nucleus. For the area of the  $i$ -th nucleus,  $A_i$ , we assume that:

$$\dot{A}_i = a S_i + b (A_{\min} - A_i). \quad (4)$$

The first term on the right-hand-side describes the growth of the nuclear area proportional to the amount of the signal,  $S_i$ , received per unit time. The second term is based on the assumption that, in the absence of any signal, the size of the nucleus approaches the minimal size,  $A_{\min}$ .

**The steady state approximation.** If we assume that the signal dynamics take place on a time scale faster than that of the nuclear growth, which is reasonable, then we can at each time step approximate (1) by its steady state solution:

$$0 = D \Delta s + \gamma \quad (x, y) \in \mathcal{C}, \quad (5)$$

and iterate between solving this steady state equation and updating the nuclear sizes according to (4). After such simulations, we observed that the amount of signal each nucleus received,  $S_i$ , depended only very mildly on its size – and thereby time – but rather depended almost exclusively on its fixed position (see Fig. M1A). This observation justifies the following procedure to determine the nuclear equilibrium sizes: 1. Set a fixed initial nuclear area for all nuclei and solve (5) with this geometry to obtain the signal concentration  $s(x, y)$ . 2. Calculate the amount of signal each nucleus receives  $S_i$  per unit time using (3). 3. Calculate the equilibrium nuclear areas as the steady state solutions to (4), i.e.

$$A_i = A_{\min} + \frac{a}{b} S_i.$$

To obtain the minimal nuclear area  $A_{\min}$  and the signal sensitivity  $\alpha = a/b$ , we solved the associated least-squares problem of the overdetermined system, i.e. we determined  $A_{\min}$  and  $\alpha$  so that the error between the measured and predicted nuclear areas in the Euclidean norm becomes minimal. This yielded  $A_{\min} = 83\mu\text{m}^2$  and  $\alpha = 0.044\mu\text{m}^2$  per unit signal. The average relative error between the predicted and actual nuclear area was 16.9%.

Note that setting  $D = \gamma = 1$  does not affect the result, and so we used these parameters and methods to obtain the results shown in all modeling figures in the main text. For the simulations, we used the Finite Element Method with quadratic elements and the adaptive mesh solver provided by Matlab’s PDE Toolbox. We used the actual measured cellular outlines, positions and number of nuclei for 200 wild-type cells.

**Results and interpretation.** In our space-sensing model, the total amount of the signal produced (and hence also absorbed) per unit time is proportional to the total cell area. Since we assume a linear dependence of the nuclear area on the amount of the signal received, the total predicted nuclear area increases linearly with cell area, as reported in the main text, Fig. 2G. However, our model goes beyond this cell-wide regulation of the nuclear area, since it suggests a mechanism for a local regulation of nuclear areas within each cell. This local regulation is evident in the experimental data if we normalize both nuclear areas and Voronoi areas by their per-cell-averages. We found that the local differences in the nuclear areas correlate with local differences in the Voronoi areas ( $R = 0.45$ ,  $p < 0.0001$ ). The amount of signal received by each nucleus, according to our model, is highly correlated with the size of its Voronoi domain (Fig. M1B,  $R = 0.93$ ,  $p < 0.0001$ ). Our model thereby offers a mechanistic explanation for both the cell-wide and some of the within-cell variation of the observed nuclear sizes. However, our space-sensing model does not explain why we see such a large dependence of nuclear size on nuclear distance to the cell poles (main text Fig. 3G). Reasons could lie in differences in signal production and/or signal transport near the poles.

**Space-sensing for modified endoreplication.** In the main text we discussed the effect of manipulating a muscle cell’s ability to increase its DNA copy number through endoreplication. In particular we looked at mutants where endoreplication was inhibited

through a knock-down (KD) of Ctd(Dup), and mutants where endoreplication was increased through overexpression (OE) of Myc. In the following we refer to them as KD and OE cells. We used our space-sensing model to determine the minimal nuclear area  $A_{\min}$  and the signal sensitivity  $\alpha$  for KD and OE cells and found the following changes compared to the wild-type:

- For OE cells both  $A_{\min}$  and the sensitivity  $\alpha$  roughly doubled ( $A_{\min}$  increased by 106%,  $\alpha$  increased by 87%).
- For KD cells  $A_{\min}$  decreased by 11%, whereas  $\alpha$  stayed roughly the same (< 1% increase).

The differences in  $A_{\min}$  might reflect the changes in (minimal) space requirements for more/less DNA copy numbers, whereas the increased sensitivity for OE cells could mean that OE nuclei react more sensitively to received signals compared to wild-type cells.

## 2 Variants of the Space-Sensing Model

Several variants of the space-sensing model presented above are possible. As already discussed, solving the fully time-dependent problem has a negligible effect on the final result.

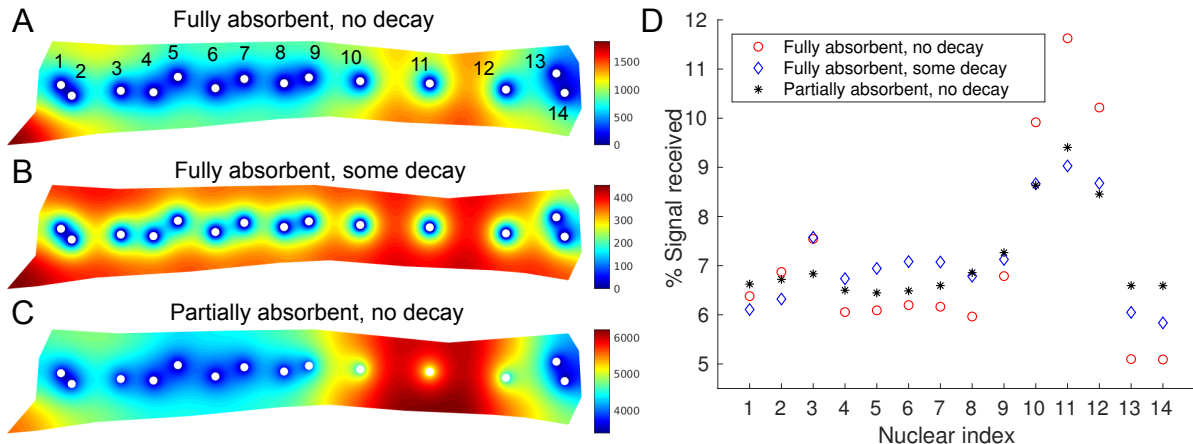


Figure M2: *A-C: Equilibrium signal distribution for three variants of the space-sensing model as described in the text. All three models use  $D = \gamma = 1$ . For A we used the basic model (fully absorbent, no decay). For B, we used  $\delta = 0.002$ , for C we used  $\sigma = 0.03$ . Note that the colorbars differ between A-C. D: Shown is the % of the total amount of absorbed signal received by each nucleus for the example cell and the models shown in A-C.*

**Signal decay.** As noted above, the amount of signal received according to the above model corresponds very well to the Voronoi areas of the nuclei. In the main text, Fig. 3F shows that the correlation between the nuclear areas and the Voronoi areas becomes sublinear for large Voronoi areas, i.e. the nuclei that are far away from their neighbors

are slightly smaller than the great size of their Voronoi areas would suggest. We tested mathematically if this could be due to a slow spontaneous decay of the molecular signal. Since, for large Voronoi areas, the signal takes longer to reach the nucleus, a greater part of the signal would decay before reaching the nucleus, compared to smaller Voronoi areas, which could explain the observed sublinearity. Mathematically, this means replacing (1) by

$$\partial_t s = D\Delta s + \gamma - \delta s \quad (x, y) \in \mathcal{C},$$

where we assume a decay rate  $\delta$  with units of per time. We tested different values of parameter  $\delta$  and found that the average relative error stayed above 16%, i.e. we could not get a significantly better prediction of the nuclear size. However, when looking at the nuclei having the largest 2% of Voronoi areas in our sample, the average relative error between simulated and measured nuclear area dropped from 30.5% to 25.0% for a moderate amount of signal decay ( $\delta = 0.0005$ ), as expected.

If the value of  $\delta$  is chosen to be too large, the prediction becomes worse, since all nuclei receive roughly the same amount of signal, independent of the space around them. Fig. M2A,C shows that away from the nuclei, the signal distribution is more even, when there is the assumed decay. Fig. M2D compares how the percentage of obtained signal varies for the two cases. As expected, signal decay leads to less variation in the signal per nucleus within a cell.

**Finite nuclear signal uptake speed.** In the model described above, we assumed that all of the signal molecules that reach a nucleus are immediately absorbed. However, it is also reasonable to assume that there is a finite absorption rate  $\sigma$ . This would change the boundary condition (2) to

$$D\nabla s \cdot n = \sigma s \quad (x, y) \in \bigcup_{i=1}^N \partial \mathcal{N}_i.$$

The original model can be seen as limiting case for  $\sigma \rightarrow \infty$ . We performed tests with different values of  $\sigma$  and found that as long as  $\sigma$  is large enough, the general result was hardly affected. We were not able to obtain significantly better fits between the calculated and the measured nuclear area by varying  $\sigma$ . Fig. M2A,C shows the different signal distribution for an example cell using finite and infinite nuclear signal uptake speed and Fig. M2D compares how the percentage of obtained signal varies for the two cases. As can be observed, finite signal changes the overall signal distribution and also leads to less variation in the signal per nucleus within a cell.

**Space-sensing in 3D.** Next, we explored how solving in three space-dimensions affects the solution. Since nuclei are positioned on one surface of the muscle cell, we can model them in the 3D setting by changing the boundary condition on that face from impenetrable (Neumann boundary condition) to fully absorbent (Dirichlet boundary condition) wherever there is a nucleus. Mathematically this means solving the following system of

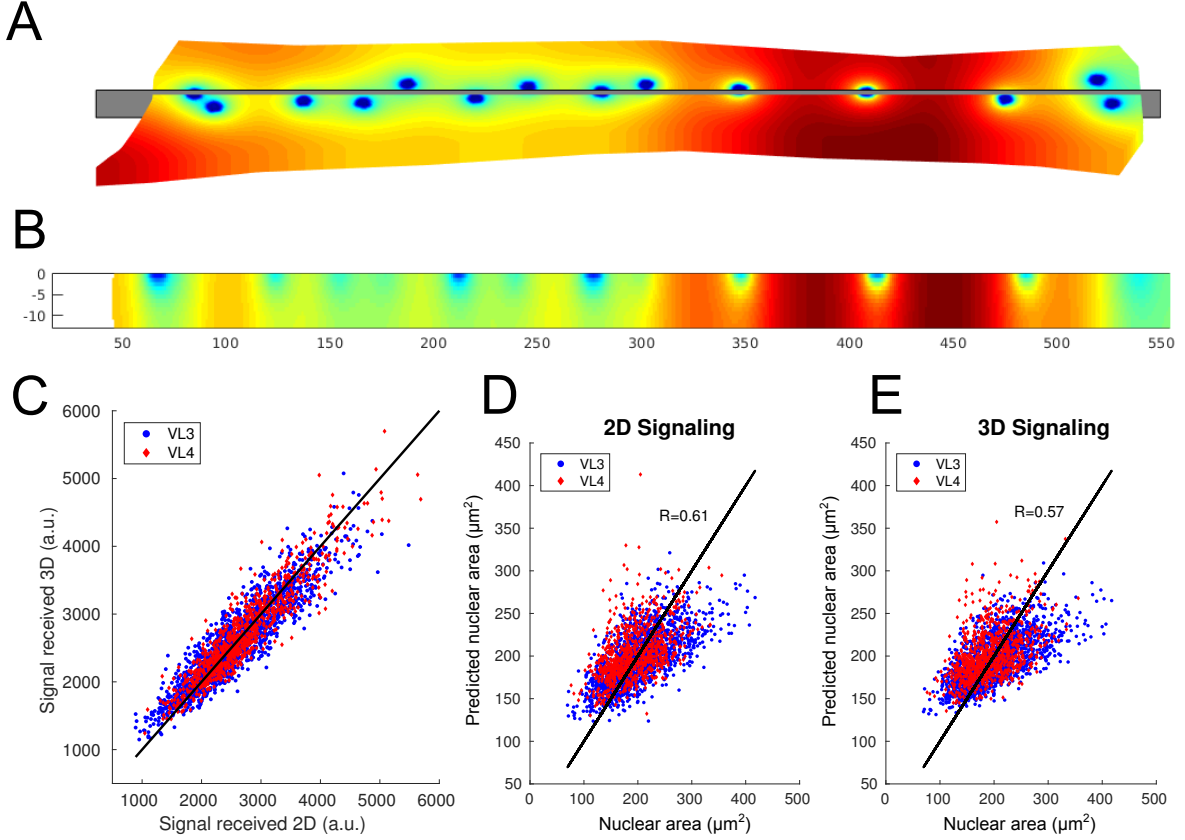


Figure M3: *A: Signal distribution on the surface of a 3D cell as described in the text. Blue = low concentration, red = high concentration. B: Slice through the cell along the plane shown in A. C: Comparing the amount of signal received for 2477 nuclei between the 2D and the 3D model. D-E: Predicted vs measured nuclear areas of the 2D and 3D model.*

equations:

$$\begin{aligned}
 0 &= D\Delta s + \gamma \quad (x, y, z) \in \mathcal{C}, \\
 \nabla s \cdot n &= 0 \quad (x, y, z) \in \partial\mathcal{C} \cap \bigcup_{i=1}^N \mathcal{N}_i, \\
 s &= 0 \quad (x, y, z) \in \bigcup_{i=1}^N \mathcal{N}_i,
 \end{aligned} \tag{6}$$

where now  $\mathcal{N}_i$  are *filled* 2D discs, representing the nuclei. Figures M3A and B show the signal distribution on the surface of the cell and along a cut through the cell, respectively. As expected, signal amounts are low near the nuclear discs. Upon comparing the amounts of signal per nucleus between the 2D and 3D simulation in Fig. M3C, we see that they are very similar. Using the amount of signal received according to the 3D simulation still allows predicting the measured nuclear area very well, however, slightly less well than using the 2D simulation. A speculative explanation could be that due to the sarcomeric structures in the cell, the diffusing signal cannot actually access the full depth of the cell.

### 3 Future Space-sensing Models

**Active signal transport.** So far the signal movement described was purely passive. However, it is possible that the signal is being transported actively, e.g. along microtubule tracks towards the nuclei or through the cell. This could be included in our model in a straight-forward manner.

**Space-sensing in mammalian muscle cells.** The geometry of mammalian skeletal muscles differs significantly from those of the fruit fly cells that we studied. Mammalian skeletal muscle cells form long, thin cylinders which contain myofibrils, within which the force-generating sarcomers are located. Muscle nuclei are positioned near the outer surface of the cylinder. Previous work [1] suggests that the position of the nuclei is consistent with a repulsion model similar to that presented in the main text. Our space-sensing model could be easily adapted to mammalian muscles, when data on correlations between nuclear sizes and spacing in such muscles become available. The different geometry could lead to different scaling laws: For example the signaling molecule could be diffusing in the full 3D cylinder or merely close to its 2D surface. Additionally, signal uptake could cause a linear increase in either nuclear volume or surface area, and finally also signal leakage from the nuclei could affect potential scaling laws.

## References

- [1] Bruusgaard J, Liestøl K, Ekmark M, Kollstad K, Gundersen K. Number and spatial distribution of nuclei in the muscle fibres of normal mice studied in vivo. *J of Physiol.* 2003;551(2):467–478.